EXPERIMENTAL AND COMPUTATIONAL STUDIES OF HYDROPHOBIC ASSOCIATION AND ION AFFINITY FOR MOLECULAR OIL/WATER INTERFACES

by

Andres S. Urbina

A Dissertation

Submitted to the Faculty of Purdue University

In Partial Fulfillment of the Requirements for the degree of

Doctor of Philosophy

Department of Chemistry

West Lafayette, Indiana

May 2022

THE PURDUE UNIVERSITY GRADUATE SCHOOL
STATEMENT OF COMMITTEE APPROVAL

Dr. Dor Ben-Amotz, Chair

Department of Chemistry

Dr. Lyudmila Slipchenko

Department of Chemistry

Dr. Nikolai Skrynnikov

Department of Chemistry

Dr. Adam Wasserman

Department of Chemistry

Approved by:

Dr. Christine A. Hrycyna

To Alba, Andres, and Francisco.

ACKNOWLEDGMENTS

I would like to thank my advisor, Prof. Dor Ben-Amotz, for his guidance and encouragement which has helped me develop as a scientist. Also, I am grateful to my co-advisor, Prof. Lyudmila Slipchenko, for her time, patience, enthusiasm, and knowledge regarding molecular simulations. I would like to acknowledge my committee members, Prof. Nikolai Skrynnikov and Prof. Adam Wasserman, for their patience and help through this process.

I am grateful to Prof. Thomas Markland, Tobias Morawietz, Xiangen Wu, and Prof. Wanjun Lu for our investigation on pure water. Also, I thank Victoria Boulos, Denilson Mendes de Oliveira, and Dr. Matthias Zeller for their contributions to our paper on the conformational changes of 1-bromopropane, and to Yongbin Kim for his insights on EFP methods.

Finally, I thank my friends for their encouragement and the many memories we have made. Most importantly, a special thank you to my family who have always been there for me.

TABLE OF CONTENTS

LIST OF TABLES

LIST OF FIGURES

ABSTRACT

Experimental and computational techniques are used to study physico-chemical phenomena occurring in water on which hydrophobic interactions play a role. In particular, hydrophobic self-aggregation, including host-guest binding, and the affinity of ions to oil/water interfaces are investigated. Raman multivariate curve resolution (Raman-MCR) spectroscopy was the experimental technique used to unveil intermolecular interactions through the analysis of solute-correlated (SC) vibrational spectra. Molecular simulations, including molecular dynamics (MD) simulations, quantum-mechanical calculations, or a combination of both, were carried out to assist with the molecular-level interpretation of the experimental SC spectra.

CHAPTER 1. EXPERIMENTAL AND COMPUTATIONAL METHODS

1.1 Raman Spectroscopy

Raman spectroscopy is an analytical technique which typically probes the vibrational states of molecular systems. It is based in the interaction of light with molecules on a phenomenon known as inelastic or Raman scattering. Specifically, a very minuscule number of photons of monochromatic light excite molecular vibrations of molecules, which ultimately relax and emit photons with frequencies different to that of the incident light. The frequencies of these inelastically scattered photons can be either lower (Stokes scattering) or higher (anti Stokes scattering) than the frequency of the incident light. The rest of the incident photons also produce vibrationally excited molecules, which after relaxation, emit photons with the same (Rayleigh scattering) frequency as that of the excitation photons.

1.2 Instrumentation

The Raman spectra reported herein were obtained using a home-built Raman system described in previous publications.[1-3] In short, it was comprised of an Ar-ion laser source (514.5 nm), a thermoelectrically cooled charge coupled device (CCD) camera (Pixis 400, 1340×400 pixels, Princeton Instruments Inc.) coupled to an imaging spectrograph (SpectraPro300i, Acton Research Inc.) with a 300 grooves/mm grating which produced a dispersion of ~5 cm^{-1}/CCD pixel. The laser light (~20 mW) was focused on the center of a 1 cm sample cell (glass cuvette, round glass vial, or glass capillary tube) using a 20× microscope objective (Mitutoyo Inc.). The Stokes Raman scattered photons were collected with the same optical path used for the incoming laser beam and transferred to the spectrograph using a fiber bundle consisting of seven (100 μm core diameter) fibers arranged in a circular array at the collection end and in a linear stack at the detection end. Additionally, this system included a temperature-controlled sample holder which kept the set temperature within ±0.01 °C. In the sample holder, each sample, except those in a glass cuvette, was housed in a 1 cm square copper block.

A Ne discharge lamp, coupled with a band pass filter, was used such that a reference emission line appeared in every spectrum. This line was used to adjust the spectra, so the Ne emission lines overlapped at identical wavelengths. The spectra were shifted in order to correct for

sub-pixel wavelength shifts generated by atmospheric pressure changes occurring during acquisition.

At the end of each experiment, a wavelength calibration was performed by collecting the emission spectrum of a Ne discharge lamp. The calibration procedure involved correlating known wavelengths of six neon peaks to the corresponding CCD pixel number using a third order polynomial. The calibration equation was used to calculate the wavelength for each CCD pixel and the wavelengths were then converted into wavenumbers using Equation 1.

$$\tilde{\nu} = \frac{10^7 \text{nm}}{1 \text{ cm}} \left(\frac{1}{\lambda_{ex}} - \frac{1}{\lambda} \right) \tag{1-1}$$

where λ_{ex} and λ are the wavelength of the excitation laser and the wavelength of the Raman scattered photons expressed in nm, respectively.

1.3 Multivariate Curve Resolution

Multivariate Curve Resolution (MCR) refers to a set of algorithms used to decompose a matrix D (m × n) into two matrices C (m × k) and S^T (k × n) according to Equation 2:

$$D = CS^T + E \tag{1-2}$$

D corresponds to a matrix that encompasses m mixtures, S^T is a matrix containing k pure components, and C is a matrix with the associated concentration profiles. E (m × n) is the residual error matrix.

The underlying principle behind all MCR methods is the Beer-Lambert law.[4] According to it, any mixture of components yields a spectrum that is a linear combination of the spectra of the pure components.

MCR methods do not need prior information about the components present in the mixture. Nevertheless, constraints associated with physical or chemical assumptions of the spectra can be considered. For instance, a characteristic constraint among MCR methods is the non-negativity of spectral components and concentration profiles. The end goal of the constraints is to reduce

intensity and rotational ambiguities. Both ambiguities can be understood by rewriting Equation 2 into:

$$D = C\left(RR^{-1}\right)S^{T} + E \tag{1-3}$$

where $C' = CR$ and $S'^{T} = R^{-1}S^{T}$. Rotational ambiguities include all the possible outcomes for C' and S'^{T} that are rotationally equivalent to C and S^{T}. If R is a diagonal matrix, intensity ambiguities occur.[5]

Self-Modeling Curve Resolution (SMCR) was the chosen MCR algorithm. It consists of an initial singular value decomposition (SVD) matrix factorization, followed by consecutive rotations such that the final matrix S^{T} comprises non-negative elements only. A detailed description of this procedure can be found in the pioneer work of Lawton and Sylvestre.[6]

1.4 Raman-MCR Spectroscopy

The decomposition of high signal-to-noise Raman spectra of two-component mixtures using the SMCR algorithm is an experimental technique called Raman-MCR spectroscopy.[7] In the Ben-Amotz group, we have extensively used it to investigate pure water and aqueous mixtures to provide insights on physico-chemical phenomena happening in water which are of interest for biological applications. Regarding aqueous mixtures, we have focused our interest on open questions about the hydration of oily molecules, gases, and ions, ranging from protons to surfactants, as well as their intermolecular interactions.[7] In particular, the studies presented in this dissertation address how they affect hydrophobic association, including host-guest binding, and the affinity of ions for molecular oil/water interfaces.

Raman-MCR provides a means of decomposing the Raman spectrum of a solution into solvent and solute-correlated (SC) spectral components.[1,6] The solvent component is constrained to the measured spectrum of the solvent which is usually pure water. The SC component contains vibrational bands of the solute itself, as well as those arising from solute perturbations into the solvent. Figure 1.1 (a) shows a decomposition performed in a high signal-to-noise Raman spectrum of a 1 mol L^{-1} *tert*-butyl alcohol solution. The differences between the spectrum of the solution and that of pure water (solvent) are the presence of the vibrational modes of TBA and a minor

decrease in intensity of the O−H stretch band. The perturbation of the solute into the solvent appears in the SC spectrum in the O−H stretch band and can be better seen in Figure 1.1 (b). The SC spectrum shown is a minimum area spectrum with non-negative features in this region. Notice that for this particular TBA concentration there are clear differences between the O−H vibrational band in the SC spectrum with that of pure water. The shape of this band is different for both spectra. In specific the SC spectrum has a peak at ∼3200 cm^{-1} which is more intense than the peak at ∼3400 cm^{-1} which is opposite to the shape observed in the spectrum of pure water. The feature near 3200 cm^{-1} is connected to water molecules making an ordered tetrahedral structure; therefore, in the SC spectrum is evident that that the water molecules perturbed by TBA have an enhanced tetrahedral structure. Another difference observed is the appearance of a peak near 3670 cm^{-1} in the SC spectrum which corresponds to non-hydrogen bonded O−H groups. Figure 1.1 (c) shows in orange, a representation of a TBA molecule with its hydration shell which together contribute to the features that appear in the SC spectrum.

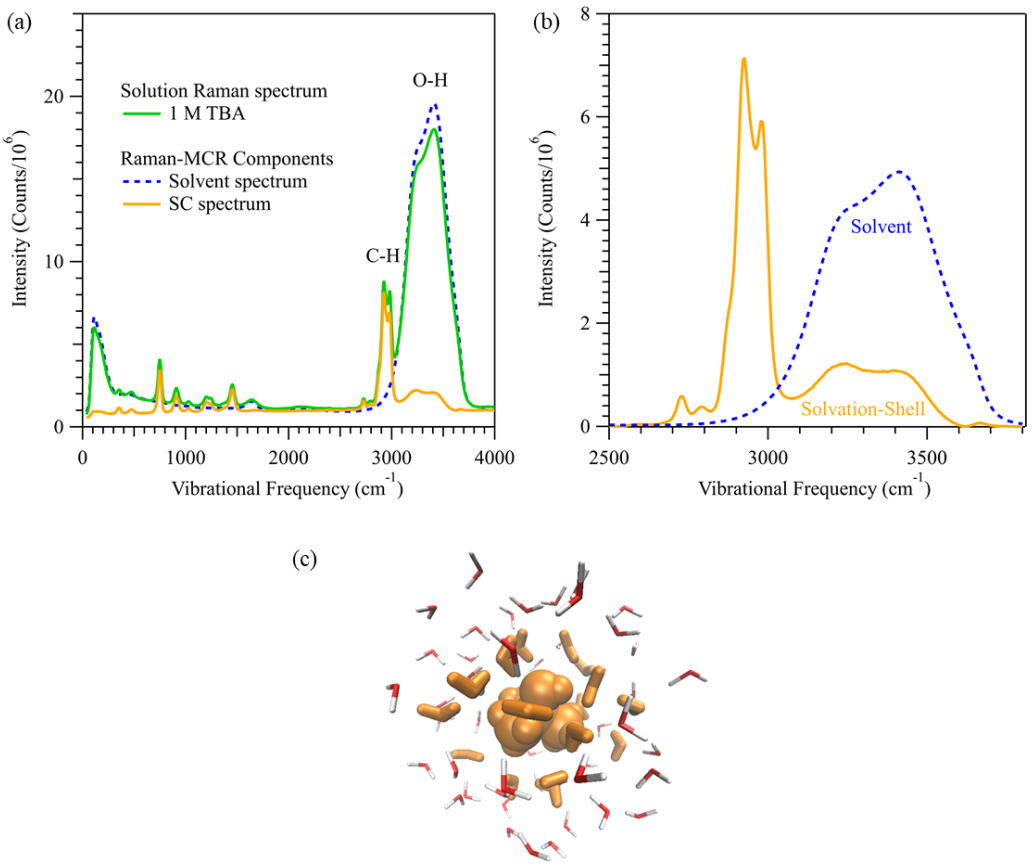

Figure 1-1. (a) Raman-MCR components of a spectrum corresponding to a 1 mol L^{-1} *tert*-butyl alcohol (TBA) solution at 20 °C. (b) Expanded view of the SC spectrum depicting the C−H and O−H stretch bands. A scaled Raman spectrum of pure water is also shown as a reference. (c) Analytes that contribute to the SC spectrum are colored in orange.

1.5 Molecular Dynamics Simulations

Molecular dynamics (MD) simulations were performed using the GROMACS package version 2019.2.[8] All boxes were generated with the corresponding GROMACS tools developed for this purpose. For each system of interest, molecules are randomly added such that they do not overlap. They are only inserted when the distance between any existing atom and any atom of the inserted molecule is less than the sum based on the van der Waals radii of both atoms. Next, an energy minimization of the total force of the system was executed, followed by an NVT equilibration. In the last step, an NPT production run was carried out. The parameters employed in the different MD steps are shown in more detail in the Methods section of Chapter 2. Regarding the classical interaction potentials, amphiphilic solutes were described by the all atom OPLS-AA force field, and for water molecules the TIP4P/2005 force field was used.[9,10,11]

Subsequent analysis of the production run trajectories was done using the in-built GROMACS tools coupled to home-built scripts.

1.6 QM-EFP Calculations

The QM-EFP refers to a hybrid methodology that couples *ab initio* methods with the Effective Fragment Potential (EFP) method. The EFP method is a quantum-mechanical based force field that allows a low-cost description of intermolecular interactions in condensed phase systems.[12,13] The evaluation of local C−H vibrations of *tert*-butyl alcohol using the QM-EFP approach is explained in more detail in the Methods section of Chapter 2.

1.7 References

(1) Davis, J. G.; Gierszal, K. P.; Wang, P.; Ben-Amotz, D., Water structural transformation at molecular hydrophobic interfaces. *Nature* **2012**, 491, 582.

(2) Mendes de Oliveira, D.; Ben-Amotz, D., Spectroscopically Quantifying the Influence of Salts on Nonionic Surfactant Chemical Potentials and Micelle Formation. *J. Phys. Chem. Lett* **2021**, 12, 355.

(3) Ben-Amotz, D.; Mendes de Oliveira, D., Surfactant aggregate size distributions above and below the critical micelle concentration. *J. Chem. Phys.* **2021**, 155, 224902.

(4) de Juan, A.; Jaumot, J.; Tauler, R., Multivariate Curve Resolution (MCR). Solving the mixture analysis problem. *Anal. Methods* **2014**, 6, 4964.

(5) Ruckebusch, C.; Blanchet, L., Multivariate curve resolution: A review of advanced and tailored applications and challenges. *Anal. Chim. Acta*. **2013**, 765, 28.

(6) Lawton, W. H.; Sylvestre, E. A., Self Modeling Curve Resolution. *Technometrics* **1971**, 13, 617.

(7) Ben-Amotz, D., Hydration-Shell Vibrational Spectroscopy. *J. Am. Chem. Soc.* **2019,** *141*, 10569.

(8) Abraham, M. J.; Murtola, T.; Schulz, R.; Páll, S.; Smith, J. C.; Hess, B.; Lindahl, E., GROMACS: High performance molecular simulations through multi-level parallelism from laptops to supercomputers. *SoftwareX* **2015**, 1-2, 19.

(9) Jorgensen, W. L.; Maxwell, D. S.; Tirado-Rives, J., Development and Testing of the OPLS All-Atom Force Field on Conformational Energetics and Properties of Organic Liquids. *J. Am. Chem. Soc.* **1996**, 118, 11225.

(10) Jorgensen, W. L.; Tirado-Rives, J., The OPLS [optimized potentials for liquid simulations] potential functions for proteins, energy minimizations for crystals of cyclic peptides and crambin. *J. Am. Chem. Soc.* **1988**, 110, 1657.

(11) Abascal, J. L. F.; Vega, C., A general purpose model for the condensed phases of water: TIP4P/2005. *J. Chem. Phys.* **2005**, 123, 234505.

(12) Gordon, M. S.; Slipchenko, L.; Li, H.; Jensen, J. H., Chapter 10 The Effective Fragment Potential: A General Method for Predicting Intermolecular Interactions. In *Annual Reports in Computational Chemistry*, Spellmeyer, D. C.; Wheeler, R., Eds. Elsevier: 2007; Vol. 3, pp 177-193.

(13) Ghosh, D.; Kosenkov, D.; Vanovschi, V.; Williams, C. F.; Herbert, J. M.; Gordon, M. S.; Schmidt, M. W.; Slipchenko, L. V.; Krylov, A. I., Noncovalent Interactions in Extended Systems Described by the Effective Fragment Potential Method: Theory and Application to Nucleobase Oligomers. *J. Phys. Chem. A* **2010**, 114, 12739.

CHAPTER 2. HYDROPHOBIC AGGREGATION OF TERT-BUTYL ALCOHOL AS REVEALED BY C–H FREQUENCY SHIFTS: AN EXPERIMENTAL AND COMPUTATIONAL STUDY

2.1 Introduction

Hydrophobic aggregation of small and large molecules in aqueous environments is of relevance to biology, pharmacy, and medicine.[1-12] Such aggregation processes may be experimentally probed using vibrational spectroscopy by, for example, measuring C–H frequency shifts upon aggregation.[13-17] However, it has still yet to be validated theoretically that C–H frequency shifts are related to hydrophobic aggregation. Here we attempt to do so by combining experiments and simulations of *tert*-butyl alcohol (TBA) dissolved in pure water. These studies combine Raman multivariate curve resolution (Raman-MCR) spectroscopy, molecular dynamics (MD) simulations, and QM-EFP frequency calculations. The MD/QM-EFP strategy used was able to reproduce the experimental C–H frequency shifts and indicates that the C–H frequency shifts are related to the local environment around a TBA molecule. Specifically, C–H frequency shifts report on the amount of neighboring TBA molecules present within the first coordination shell.

2.2 Methods

Preparation of Aqueous Solutions. Aqueous solutions of *tert*-butyl alcohol (Sigma-Aldrich, ≥ 99.7%), and d9-*tert*-butyl alcohol (CDN Isotopes, 99 atom % D) were prepared with ultrapure filtered water (Milli-Q UF Plus, Millipore, 18.2 MΩ cm).

Raman-MCR Spectroscopy. Raman spectra were obtained at 20°C using an Ar-ion 514.5 nm laser with ~20 mW of power at the sample and 5 min integration time, as previously described.[14,18] Self-modeling curve resolution (SMCR) algorithm was used on pairs of solvent and solution spectra to obtain Raman-MCR solute-correlated (SC) spectra.[13,19-21]

MD/QM-EFP Molecular Simulations. Molecular dynamics (MD) simulations were performed using the GROMACS package (version 2019.2).[22] The OPLS all atom force field (OPLS-AA) was used for the TBA molecule, whereas the TIP4P-2005 force field was used for water.[23-25] After energy minimization, NVT equilibration was performed for 200 ps, with a 1 fs time step, to ensure a plateau in density. NPT production run was carried out for 300 ns, with a 2 fs time step, a velocity

rescale thermostat for temperature control (293 K) and Parrinello−Rahman barostat for pressure control (1 bar).[26-27] Bonds were constrained with the LINCS algorithm.[28] A 1 nm cutoff was used to handle Lennard-Jones potentials. Electrostatic long-range interactions were treated with particle mesh Ewald (PME) summations with a real-space cutoff of 1 nm.[29-30] In total, 8 MD simulations were performed corresponding to concentrations of 0.27, 0.53, 1.02, 1.87, 3.26, 5.06, 7.03, and 8.59 mol L^{-1}. For each MD simulation, 200 TBA molecules were used, and the number of water molecules was adjusted to produce the aforementioned concentrations.

Each trajectory obtained was converted such that a TBA molecule is in the center of the box. Next, the snapshots of interest, on which the central TBA has k neighbors within the first coordination shell, were extracted, labeled, and grouped according to k. From these snapshots, configurations that include the central TBA and its first coordination shell were extracted. Local mode C–H frequency calculations were carried out using a hybrid QM-EFP method and partial Hessian vibrational analysis (PHVA) as implemented in the GAMESS 2018 R1 suite of programs.[31-33] The central TBA molecule of each configuration was described with the second-order Møller–Plesset perturbation theory using the 6-311++G** basis set.[34] Waters and TBA molecules present in the coordination shell were described by EFP potentials.[35-36] PHVA was done on all 9 hydrogens located in the methyl groups of TBA. For every calculation, all atoms of the central TBA molecule and fragments were held fixed, except for the hydrogen atom under investigation.

2.3 Results and Discussion

Figure 2-1 (a) depicts the SC spectra, normalized to the C–H band area, obtained from the SMCR decomposition of pairs of spectra corresponding to pure water and TBA solutions of different concentrations. Notice the depletion of the O–H band as the concentration increases which is associated to the dehydration of TBA as aggregates form. The changes that are occurring to the C–H band are not evident. Nevertheless, the overall band shifts to lower frequencies as the TBA concentration increases. The concentration dependence of the average C–H frequency is plotted in Figure 2-1 (b). It has a sigmoidal shape that is characteristic of micelle aggregation.[13-14] The C–H frequency of fully hydrated free TBA molecules is ~2944 cm^{-1}, whereas the C–H frequency of fully dehydrated TBA molecules, present in pure TBA, is ~2937 cm^{-1}. The critical aggregation concentration (cac) is approximately the concentration at which the C–H frequency

has a noticeable nonlinear dependence. The cac can be estimated from Figure 1 (b), and it has a value of ~2.5 mol L^{-1}. MCPS analysis has been also used to model the aggregation of TBA and determined that the effective cac is ~2.6 mol L^{-1}.[13] Furthermore, the nearly linear concentration dependence below cac implies that low-order aggregation is occurring in this concentration range.

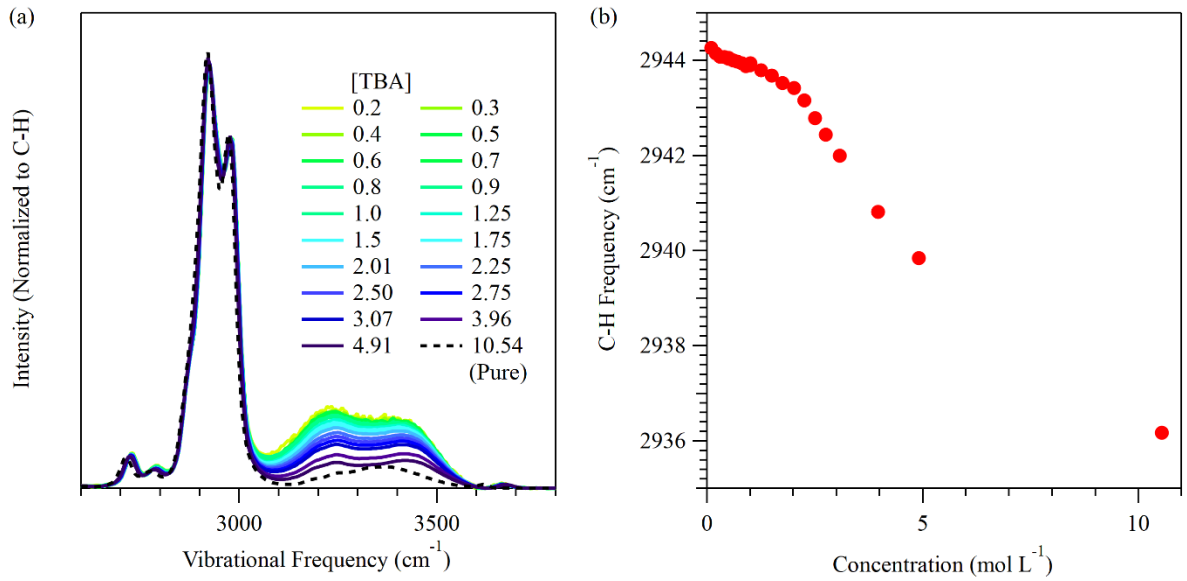

Figure 2-1. (a) Concentration-dependent Raman-MCR SC spectra obtained from pairs of spectra consisting of the pure water and the corresponding TBA solution spectra. (b) Average C–H frequency of TBA plotted as a function of concentration.

As mentioned in the Methods section, the molecular simulations performed, using a MD/QM-EFP strategy, were designed to obtain local C–H frequencies for all nine C–H moieties that exist in the three methyl groups of a TBA molecule. To compare our calculated C–H frequency shifts with those obtained from experiments, we, first, had to confirm that the experimental average C–H frequency dependence does resemble the C–H frequency dependence of a local vibration. The strategy used to confirm this hypothesis involved studying the aggregation of d9-TBA by means of Raman-MCR spectroscopy. d9-TBA was chosen since the commercially available sample was ~99% pure, thus containing ~1% of impurities. The impurities consist of H atoms that are replacing D atoms in the d9-TBA molecules. A d9-TBA molecule that include a H atom correspond to a system that contain a local C–H vibration as depicted in Figure 2-2.

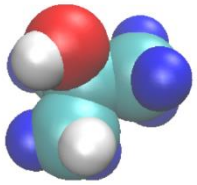

Figure 2-2. Molecular representation of a d9-TBA molecule with a H atom impurity.

Figure 2-3 (a) shows the d9-TBA SC spectra normalized to the C–D band area. Notice that the frequency range used for the SMCR decomposition was constrained such that it only included the C–D and C–H bands. This is the reason for the appearance of negative intensities in the O–H region. Notice that the C–H peak appears at ~2950 cm^{-1} and it is a fingerprint of the local C–H modes that exist in d9-TBA molecules in the different aqueous solutions. An expansion of the d9-TBA SC spectra in the C–H region is shown in Figure 2-3 (b). It includes the SC spectrum of the most diluted solution as well as the SC spectrum of the solution with a concentration close to the cac. Notice that this figure also portrays the Gaussian fitting done to these peaks in order to obtain the maximum of each fit function. The maximum of these Gaussian functions was obtained for all the solutions and plotted versus concentration, as represented in the curve formed by the black squares in Figure 2-3 (c). For comparison, Figure 2-3 (c) also includes the average C–H frequency dependence on concentration obtained for the fully non-deuterated TBA. Notice the similarity in the shapes of both the black and red curves. The concentration dependence of the average C–D frequency is plotted in Figure 2-3 (d).

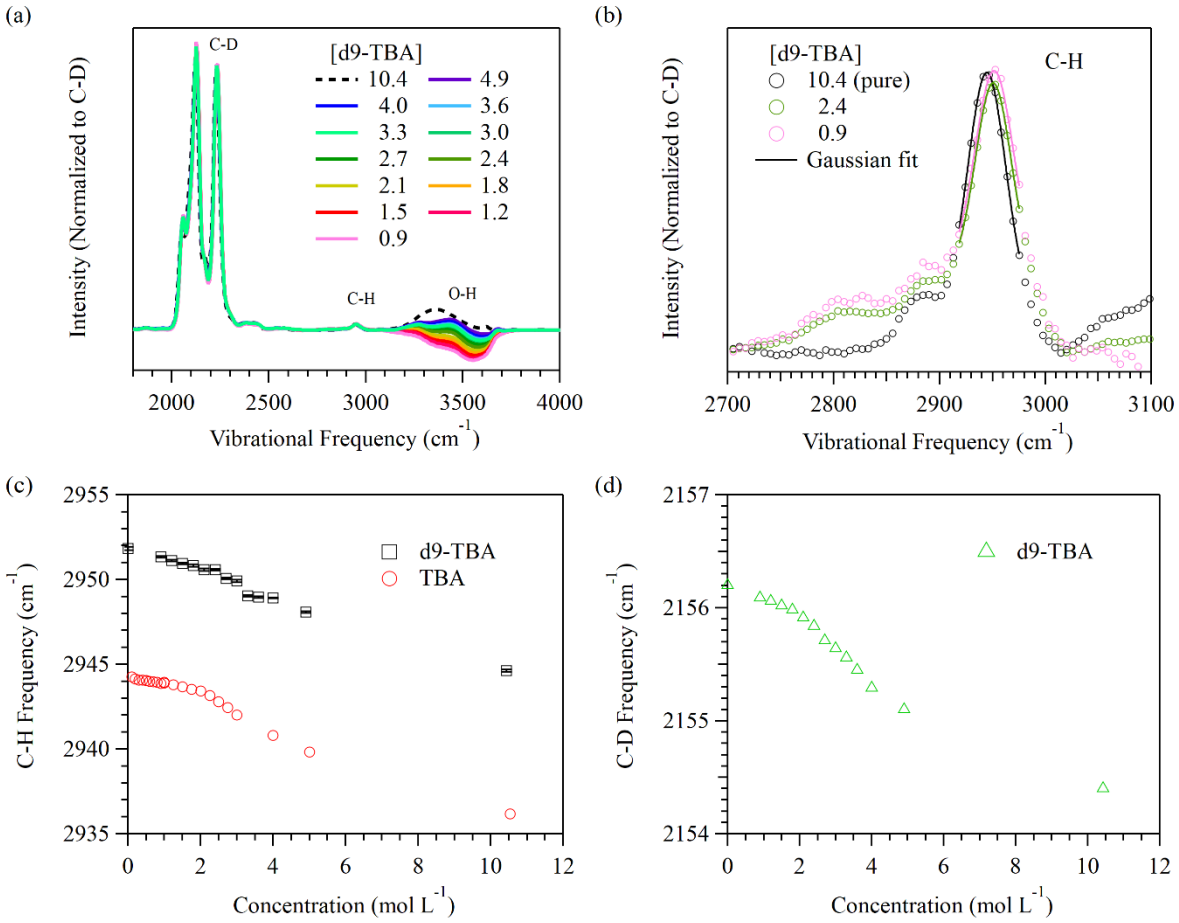

Figure 2-3. (a) Concentration-dependent Raman-MCR SC spectra of d9-TBA. (b) Expansion of (a) in the C–H region. (c) Local mode C–H frequency of d9-TBA and average C–H frequency of TBA, both plotted as a function of concentration. (d) Average C–D frequency of d9-TBA plotted as a function of concentration.

Figure 2-4 shows the frequency shifts obtained after shifting all the C–H frequencies with the corresponding dilute limit C–H frequency. The C–H frequency at the dilute limit for each curve corresponds to the intercept of a linear fit to the data points below cac. Notice that the local mode C–H frequency shift, the average C–H frequency shift, and the average C–D frequency shift have the same concentration dependence. These results confirm that both the average C–H frequency and local mode C–H frequency provide the same information. Additionally, it is demonstrated that deuteration of TBA does not have an effect on the concentration dependence.

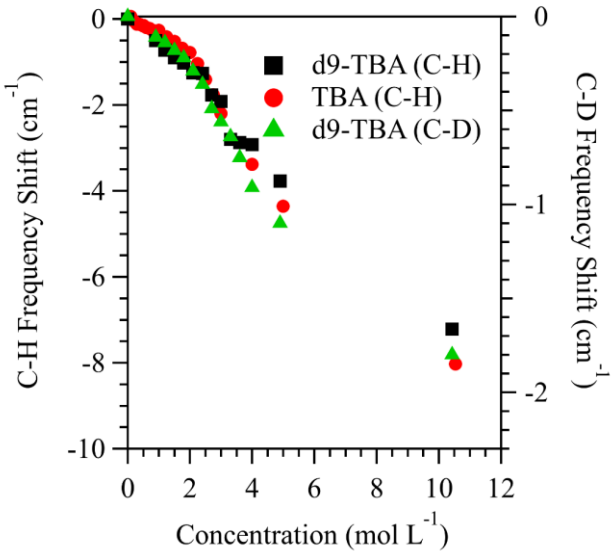

Figure 2-4. Local mode C–H frequency shift, average C–H frequency shift and average C–D frequency shift versus concentration.

Figures 2-5 (a) and (b) depict the results of the different MD simulations performed. Figure 2-5 (a) shows how many times k neighbors happen within 0.75 nm of a TBA molecule on a 300 ns trajectory that has a total of 14500 snapshots corresponding to the 1.87 mol L^{-1} MD trajectory. This cutoff corresponds to the first minimum in the radial distribution function (central C – central C) of the MD trajectory corresponding to the lowest concentration. Figure 2-5 (b) shows P(k), the normalized distribution of k contacts, for each MD system. Notice that the distribution of contacts changes smoothly at low and high concentrations. However, there is a drastic variation when the concentration changes from 1.87 mol L^{-1} to 3.26 mol L^{-1}. Notice, in specific, the increase in population for high k values when the concentration is 3.26 mol L^{-1}. This result suggests there is a local structural transition happening between these two

concentrations, which is the concentration region on which aggregates start forming according to experiments.

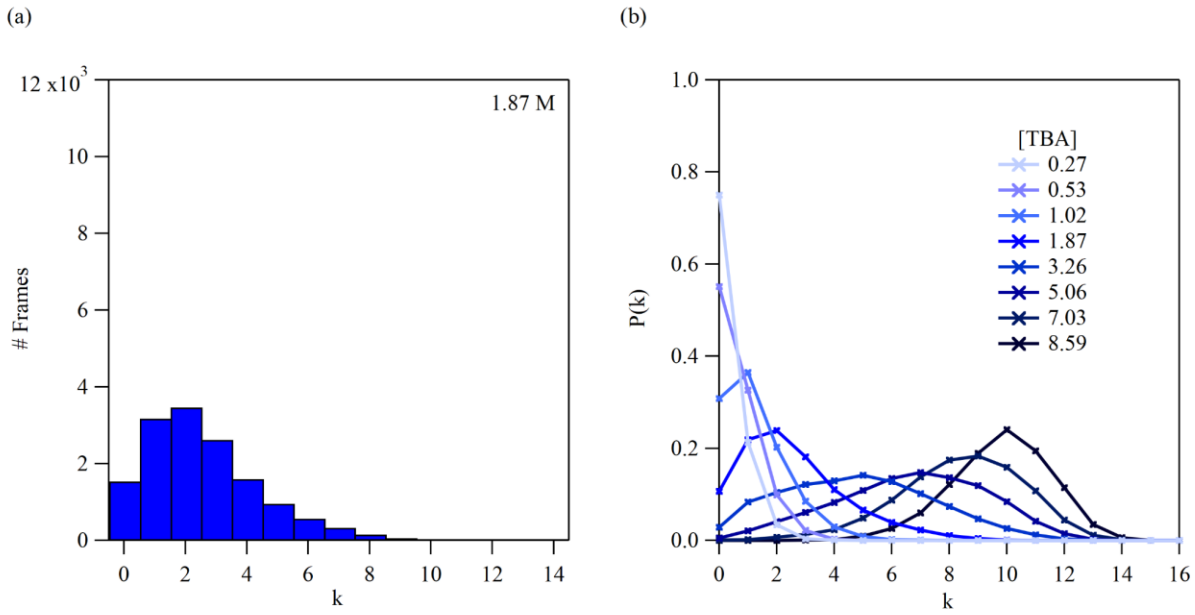

Figure 2-5. (a) Distribution of contacts around a TBA molecule for the MD trajectory corresponding to a concentration of 1.87 mol L^{-1}. (b) Normalized distribution of contacts for each MD trajectory.

The QM-EFP local-mode vibrational frequency calculations were done on 1000 configurations for each k. The configurations on which k neighbors are present within 0.75 nm of a TBA molecule were extracted from the MD trajectories on which that particular k is the most abundant. For instance, configurations where a TBA molecule has 2 neighboring TBA molecules (k = 2) were extracted from the trajectory corresponding to a concentration of 1.87 mol L^{-1}. Figures 6 (a) and (b) illustrate configurations corresponding to k = 0 and k = 2, respectively.

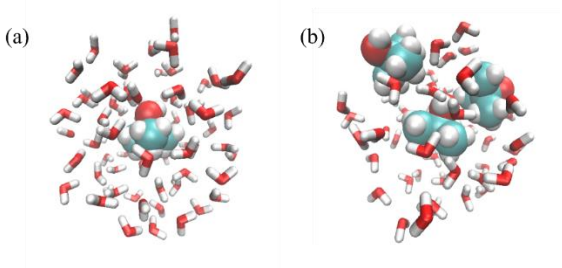

Figure 2-6. (a) Configuration where a TBA molecule does not have a TBA neighbor within 0.75 nm (k = 0). (b) Configuration where a TBA molecule has two TBA neighbors within 0.75 nm (k = 2).

Figure 2-7 (a) shows the distribution of frequencies obtained for each k. Each distribution was generated from 9000 C–H local mode frequencies that were calculated as described in the Methods section. Notice that these distributions roughly have a Gaussian shape. For each distribution, the mean, the median, and the maximum of a Gaussian fit were found and then averaged. These average C–H frequencies were plotted as a function of k as depicted in Figure 2-7 (b). Notice that the C–H frequency dependence on k is somewhat nonlinear. Additionally, the frequency shift produced when going from a fully hydrated (k = 0) configuration to a slightly hydrated (k = 10) configuration is ~7 cm^{-1}. The C–H frequency corresponding to the configuration on which k = 10 was extrapolated using the polynomial coefficients that are shown in Figure 2-7 (b). This 7 cm^{-1} shift agrees with the experimental C–H frequency shift obtained when transitioning from infinitely dilute TBA to pure TBA.

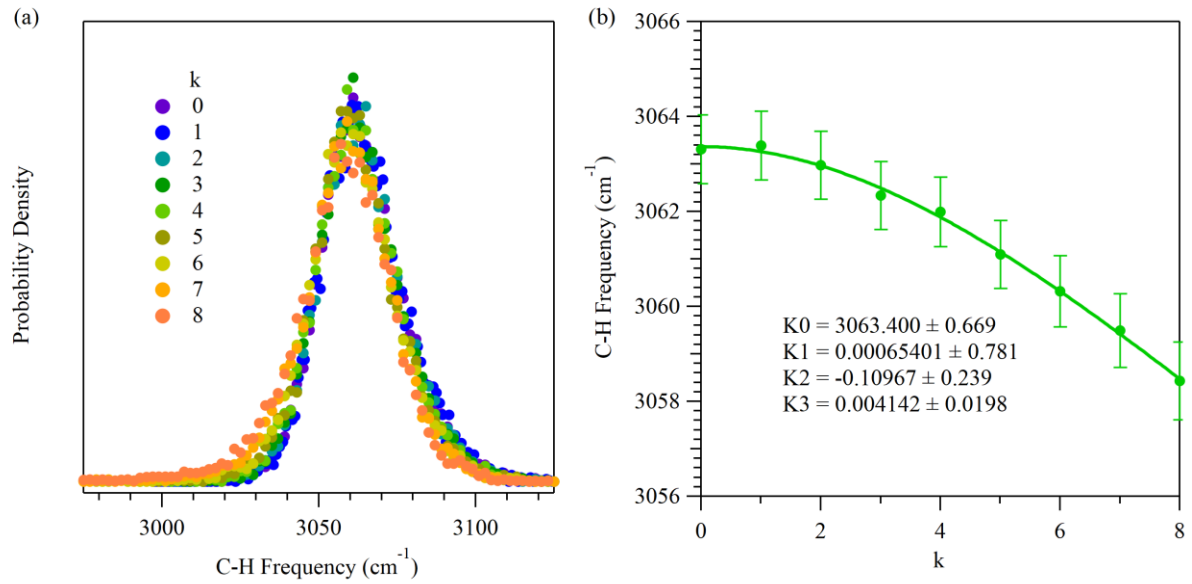

Figure 2-7. (a) C–H frequency distributions versus k. (b) C–H frequency as a function of k. The coefficients shown belong to the polynomial function (solid line) that fits the points.

To obtain the C–H frequency of a particular concentration, extrapolated C–H frequencies for each k were weighted by the corresponding P(k), which is accessible in the distribution of contacts of that concentration, and then added. Next, the calculated C–H frequencies were shifted by the C–H frequency of the fully hydrated (k = 0) configuration resulting in the C–H frequency shifts shown as black dots in Figure 2-8. Note the close agreement of the calculated C–H frequency shifts with the experimental C–H frequency shifts shown in red dots. Nevertheless, the calculated concentration profile suggests that the molecular simulations are not capturing the association happening above 5 mol L^{-1}. This can be associated to the fact that the OPLS-AA forcefield used underestimates aggregation.[36]

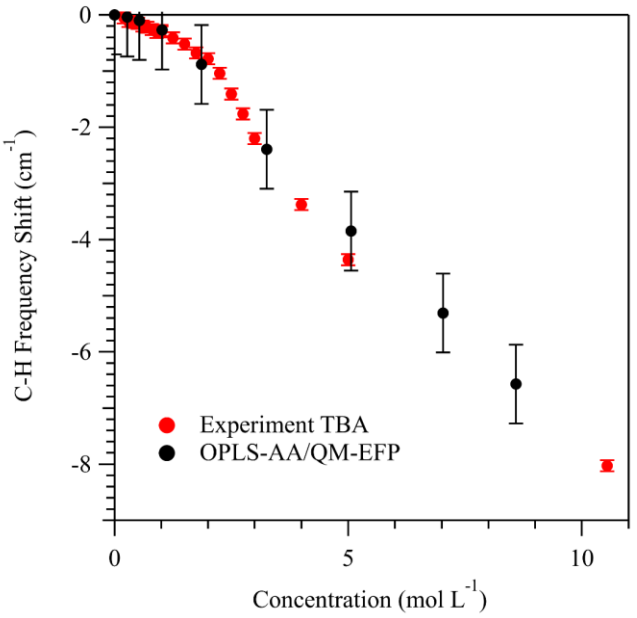

Figure 2-8. Calculated C–H frequency shifts plotted as a function of concentration. The experimental C–H frequency shifts of the fully non deuterated TBA as a function of concentration are also shown.

2.4 Conclusions

In summary, experiments and molecular simulations were used to understand the connection between C–H frequency shifts and hydrophobic self-aggregation of TBA. In specific, we used Raman MCR to obtain suitable C–H bands that allow the calculation of precise average C–H frequencies. The average C–H frequency (average normal mode C–H frequency) and local mode C–H frequency were proven to have the same concentration dependence. The experimental results obtained for d9-TBA with a local vibration inspired the molecular simulation strategy that was used. The MD/QM-EFP approach consisted of generating the environment that a TBA molecule could have in a real aqueous solution with MD simulations, extraction of configurations that include a TBA molecule with its coordination shell, and QM-EFP local-mode vibrational frequency calculations on each C–H group of the central TBA molecule. The calculated C–H frequencies have a slightly non-linear dependence on the number of neighbors that are included within the coordination shell. The calculated C–H frequency shifts as a function of concentration reproduce the C–H frequency shifts observed experimentally. The MD/QM-EFP molecular simulations suggest that C–H frequency shifts are related to the average number of TBA contacts around a TBA molecule. Hence, C–H frequency shifts report the local aggregation happening

around a TBA molecule as concentration is increased. The connection of C–H frequencies and average number of contacts to the formation of microheterogeneities, as suggested by large scale MD simulations, has still yet to be investigated.[37-39]

2.5 References

(1) Tanford, C., The Hydrophobic Effect and the Organization of Living Matter. *Science* **1978**, 200, 1012.

(2) Chandler, D., Interfaces and the driving force of hydrophobic assembly. *Nature* **2005**, 437, 640.

(3) Jiang, L.; Cao, S.; Cheung, P. P.-H.; Zheng, X.; Leung, C. W. T.; Peng, Q.; Shuai, Z.; Tang, B. Z.; Yao, S.; Huang, X., Real-time monitoring of hydrophobic aggregation reveals a critical role of cooperativity in hydrophobic effect. *Nat. Commun.* **2017**, 8, 15639.

(4) Ball, P., Water as an Active Constituent in Cell Biology. *Chem. Rev.* **2008**, 108, 74.

(5) LaPlante, S. R.; Aubry, N.; Bolger, G.; Bonneau, P.; Carson, R.; Coulombe, R.; Sturino, C.; Beaulieu, P. L., Monitoring Drug Self-Aggregation and Potential for Promiscuity in Off-Target In Vitro Pharmacology Screens by a Practical NMR Strategy. *J. Med. Chem.* **2013**, 56, 7073.

(6) Frenkel, Y. V.; Clark, A. D.; Das, K.; Wang, Y.-H.; Lewi, P. J.; Janssen, P. A. J.; Arnold, E., Concentration and pH Dependent Aggregation of Hydrophobic Drug Molecules and Relevance to Oral Bioavailability. *J. Med. Chem.* **2005**, 48, 1974.

(7) Owen, S. C.; Doak, A. K.; Wassam, P.; Shoichet, M. S.; Shoichet, B. K., Colloidal Aggregation Affects the Efficacy of Anticancer Drugs in Cell Culture. *ACS Chem. Biol.* **2012**, 7, 1429.

(8) Coan, K. E. D.; Maltby, D. A.; Burlingame, A. L.; Shoichet, B. K., Promiscuous Aggregate-Based Inhibitors Promote Enzyme Unfolding. *J. Med. Chem.* **2009**, 52, 2067.

(9) LaPlante, S. R.; Carson, R.; Gillard, J.; Aubry, N.; Coulombe, R.; Bordeleau, S.; Bonneau, P.; Little, M.; O'Meara, J.; Beaulieu, P. L., Compound Aggregation in Drug Discovery: Implementing a Practical NMR Assay for Medicinal Chemists. *J. Med. Chem.* **2013**, 56, 5142.

(10) Chiesa, G.; Kiriakov, S.; Khalil, A. S., Protein assembly systems in natural and synthetic biology. *BMC Biol.* **2020**, 18, 35.

(11) Wilson, C. J.; Bommarius, A. S.; Champion, J. A.; Chernoff, Y. O.; Lynn, D. G.; Paravastu, A. K.; Liang, C.; Hsieh, M.-C.; Heemstra, J. M., Biomolecular Assemblies: Moving from Observation to Predictive Design. *Chem. Rev.* **2018**, 118, 11519.

(12) Banani, S. F.; Lee, H. O.; Hyman, A. A.; Rosen, M. K., Biomolecular condensates: organizers of cellular biochemistry. *Nat. Rev. Mol. Cell Biol.* **2017**, 18, 285.

(13) Ben-Amotz, D.; Mendes de Oliveira, D., Surfactant aggregate size distributions above and below the critical micelle concentration. *J. Chem. Phys.* **2021**, 155, 224902.

(14) Mendes de Oliveira, D.; Ben-Amotz, D., Spectroscopically Quantifying the Influence of Salts on Nonionic Surfactant Chemical Potentials and Micelle Formation. *J. Phys. Chem. Lett.* **2021**, 12, 355.

(15) Wilcox, D. S.; Rankin, B. M.; Ben-Amotz, D., Distinguishing aggregation from random mixing in aqueous t-butyl alcohol solutions. *Faraday Discuss.* **2013**, 167, 177.

(16) Hajji, S. M.; Errahmani, M. B.; Coudert, R.; Durand, R. R.; Cao, A.; Taillandier, E., A comparative study of 1,2-hexanediol and 1,2,3-octanetriol in aqueous solutions by different physical techniques. *J. Phys. Chem.* **1989**, 93, 4819.

(17) Yang, P. W.; Mantsch, H. H., The critical micellization temperature and its dependence on the position and geometry of the double bond in a series of sodium octadecenoates. *J. Colloid Interface Sci.* **1986**, 113, 218.

(18) Davis, J. G.; Gierszal, K. P.; Wang, P.; Ben-Amotz, D., Water structural transformation at molecular hydrophobic interfaces. *Nature* **2012**, 491, 582.

(19) Perera, P.; Wyche, M.; Loethen, Y.; Ben-Amotz, D., Solute-Induced Perturbations of Solvent-Shell Molecules Observed Using Multivariate Raman Curve Resolution. *J. Am. Chem. Soc.* **2008**, 130, 4576.

(20) Ben-Amotz, D., Hydration-Shell Vibrational Spectroscopy. *J. Am. Chem. Soc.* **2019**, 141, 10569.

(21) Lawton, W. H.; Sylvestre, E. A., Self Modeling Curve Resolution. *Technometrics* **1971**, 13, 617.

(22) Abraham, M. J.; Murtola, T.; Schulz, R.; Páll, S.; Smith, J. C.; Hess, B.; Lindahl, E., GROMACS: High performance molecular simulations through multi-level parallelism from laptops to supercomputers. *Softwarex* **2015**, 1-2, 19.

(23) Jorgensen, W. L.; Maxwell, D. S.; Tirado-Rives, J., Development and Testing of the OPLS All-Atom Force Field on Conformational Energetics and Properties of Organic Liquids. *J. Am. Chem. Soc.* **1996**, 118, 11225.

(24) Jorgensen, W. L.; Tirado-Rives, J., The OPLS [optimized potentials for liquid simulations] potential functions for proteins, energy minimizations for crystals of cyclic peptides and crambin. *J. Am. Chem. Soc.* **1988**, 110, 1657.

(25) Abascal, J. L. F.; Vega, C., A general purpose model for the condensed phases of water: TIP4P/2005. *J. Chem. Phys.* **2005**, 123, 234505.

(26) Bussi, G.; Donadio, D.; Parrinello, M., Canonical sampling through velocity rescaling. *J. Chem. Phys.* **2007**, 126, 014101.

(27) Parrinello, M.; Rahman, A., Polymorphic transitions in single crystals: A new molecular dynamics method. *J. Appl. Phys.* **1981**, 52, 7182.

(28) Mackerell Jr, A. D.; Feig, M.; Brooks III, C. L., Extending the treatment of backbone energetics in protein force fields: Limitations of gas-phase quantum mechanics in reproducing protein conformational distributions in molecular dynamics simulations. *J. Comput. Chem.* **2004**, 25, 1400.

(29) Darden, T.; York, D.; Pedersen, L., Particle mesh Ewald: An N·log(N) method for Ewald sums in large systems. *J. Chem. Phys.* **1993**, 98, 10089.

(30) Essmann, U.; Perera, L.; Berkowitz, M. L.; Darden, T.; Lee, H.; Pedersen, L. G., A smooth particle mesh Ewald method. *J. Chem. Phys.* **1995**, 103, 8577.

(31) Li, H.; Jensen, J. H., Partial Hessian vibrational analysis: the localization of the molecular vibrational energy and entropy. *Theor. Chem. Acc.* **2002**, 107, 211.

(32) Ghysels, A.; Van Speybroeck, V.; Pauwels, E.; Catak, S.; Brooks, B. R.; Van Neck, D.; Waroquier, M., Comparative study of various normal mode analysis techniques based on partial Hessians. *J. Comput. Chem.* **2010**, 31, 994.

(33) Barca, G. M. J.; Bertoni, C.; Carrington, L.; Datta, D.; De Silva, N.; Deustua, J. E.; Fedorov, D. G.; Gour, J. R.; Gunina, A. O.; Guidez, E.; et al. Recent Developments in the General Atomic and Molecular Electronic Structure System. *J. Chem. Phys.* **2020**, 152, 154102.

(34) Frisch, M. J.; Pople, J. A.; Binkley, J. S., Self-consistent molecular orbital methods 25. Supplementary functions for Gaussian basis sets. *J. Chem. Phys.* **1984**, 80, 3265-3269.

(35) Hands, M. D.; Slipchenko, L. V., Intermolecular Interactions in Complex Liquids: Effective Fragment Potential Investigation of Water–tert-Butanol Mixtures. *J. Phys. Chem. B* **2012**, 116, 2775.

(36) Flick, J. C.; Kosenkov, D.; Hohenstein, E. G.; Sherrill, C. D.; Slipchenko, L. V., Accurate Prediction of Noncovalent Interaction Energies with the Effective Fragment Potential Method: Comparison of Energy Components to Symmetry-Adapted Perturbation Theory for the S22 Test Set. *J. Chem. Theory Comput.* **2012**, 8, 2835.

(37) Gupta, R.; Patey, G. N., Aggregation in dilute aqueous tert-butyl alcohol solutions: Insights from large-scale simulations. *J. Chem. Phys.* **2012**, 137, 034509.

(38) Overduin, S. D.; Perera, A.; Patey, G. N., Structural behavior of aqueous t-butanol solutions from large-scale molecular dynamics simulations. *J. Chem. Phys.* **2019**, 150, 184504.

(39) Overduin, S. D.; Patey, G. N., Comparison of simulation and experimental results for a model aqueous tert-butanol solution. *J. Chem. Phys.* **2017**, 147, 024503.

CHAPTER 3. BINDING-INDUCED UNFOLDING OF 1-BROMOPROPANE IN ALPHA-CYCLODEXTRIN

A version of this chapter was published in a peer-reviewed journal as:
Urbina, A. S.; Boulos, V. M.; Mendes de Oliveira, D.; Zeller, M.; Ben-Amotz, D., Binding Induced Unfolding of 1-Bromopropane in α-Cyclodextrin. *J. Phys. Chem. B* **2020**, *124*, 48, 11015-11021.

3.1 Introduction

Binding-induced conformational changes play an important role in a wide range of biochemical and pharmaceutical processes,[1-7] although the conventional lock-and-key picture of host-guest binding implicitly neglects the influence of conformational flexibility on binding affinity. Some previous experimental and theoretical studies have reported evidence of guest conformational changes upon binding to a host cavity[6-10] but have not quantified the associated binding-induced conformational equilibrium constant and thermodynamic changes or compared the corresponding complex structures in the solid and aqueous solution states. Here, we do so by performing Raman multivariate curve resolution (Raman-MCR) and X-ray crystallographic measurements of the binding of 1-bromopropane (1-BP) to α-cyclodextrin (α-CD). Our results reveal that the guest *gauche*−*trans* conformational equilibrium shifts toward the *trans* conformer upon binding (although both conformers are present in the bound complex) and is essentially the same in the solid and aqueous systems. Moreover, temperature-dependent Raman measurements of the solid complex reveal that the binding-induced unfolding of 1-BP is both enthalpically and entropically favored. Thus, the present results provide a quantitative illustration of the importance of relaxing the simple lock-and-key picture of host-guest binding to include conformational flexibility and the associated entropic contributions to binding affinities.

Several previous studies of guest conformation changes have involved synthetic nanocapsule hosts. These include NOESY and COSY nuclear magnetic resonance (NMR) experimental and molecular dynamics simulation studies of the folding and helix formation of long alkanes trapped in cavitand nanocapsule complexes and nanotubes.[9-13] Cyclodextrins, which are biologically produced hosts widely used in drug delivery and other supramolecular assembly applications,[14-16] have also been found to induce guest conformational changes,[17] probed using various NMR methods[18,19] and vibrational spectroscopy.[20,21]

Raman-MCR provides a means of decomposing the Raman spectrum of a solution into solvent and solute-correlated (SC) spectral components. The latter SC component contains intramolecular solute vibrational bands, as well as more subtle information arising from solute-solvent interactions and conformational flexibility, including changes in *gauche-trans* equilibrium constants.[22] The present Raman-MCR measurements are facilitated by the fact that the *gauche* and *trans* conformers have well-resolved C−Br stretch peaks near 560 and 640 cm^{-1}, respectively.[23] Unlike prior studies that have used Raman-MCR to measure solute hydration-shell O−H band spectra,[24] here we use binding-induced changes in the guest C−Br and C−H stretch band intensities to both confirm host−guest binding and quantify binding-induced changes in the 1-BP *gauche-trans* equilibrium. More specifically, SC spectra of the free and bound aqueous host and guest molecules have been obtained using self-modeling curve resolution (SMCR)[22,24-27] (see the Methods section for further details).

3.2 Methods

Preparation of Aqueous Solutions. Saturated aqueous solutions of 1-BP (99.5+%, Sigma-Aldrich) were prepared by gently adding 2 mL of water (18.2 MΩ cm resistivity, Milli-Q UF Plus) or a 20 mM aqueous solution of α-CD (99.5+%, TCI) into a glass cuvette that already contained 50 μL of 1-BP. Thus, all saturated 1-BP solutions contained two liquid phases consisting of a 1-BP-rich droplet (at the bottom of the cell) surrounded by the aqueous phase and stored for at least 48 h in order to allow 1-BP to saturate the aqueous phase to its solubility limit of approximately 20 mmol L^{-1} free 1-BP.[28] When the aqueous solution contained α-CD, after sitting for 3 days or more, crystals of different sizes were observed to grow at the meniscus between the aqueous and 1-BP phases.

Raman Spectroscopy. Unless stated otherwise, two replicate 5 min spectra were obtained using a 514.5 nm Ar-ion excitation laser with ∼20 mW at the sample, as previously described.[26] Liquid and gas samples (in a 12 mm round glass vial) and pure α-CD powder (in a melting-point capillary) were tightly fit within a 1 cm copper block held at 20 °C, and crystals of the α-CD-1-BP complex were mounted on the copper block. Pure liquid and solid spectra were obtained using two 1 min replicates.

Raman-MCR. SMCR[25] was used to decompose solution and solvent spectra into solvent and SC components.[22,24,26,27] The SC spectrum of saturated 1-BP in an aqueous 20 mmol L^{-1} α-CD were obtained using an aqueous 20 mmol L^{-1} α-CD solution as the solvent reference spectrum.

Single-Crystal X-ray Diffraction. A suitable single crystal (∼0.4 mm^3) of the α-CD-1-BP complex was taken directly from the biphasic crystallization setup, quickly coated with a trace of Fomblin oil, and transferred directly into the cold stream of a goniometer head of a Bruker QUEST diffractometer with a fixed chi angle, a Mo Kα wavelength (λ = 0.71073 Å) sealed fine focus X-ray tube, a single-crystal curved graphite incident beam monochromator, and a PHOTON 100 CMOS area detector equipped with an Oxford Cryosystems low-temperature device. Examination and data collection were performed at 150 K (see the Supporting Information for further details).

Density Functional Theory Calculations. Density functional theory (DFT) calculations of different 1-BP systems were performed using the Gaussian 16 suite of programs.[29] Geometry optimizations along with Raman spectra were calculated. For the bound 1-BP species, geometries of 1:1 complexes were taken from the most probable configurations, as obtained from the X-ray diffraction measurements for each conformer. Two levels of theory were used, B3LYP/6-31g(d,p) and WB97/LANL2DZ. The systems studied and the corresponding results are shown in Tables 3-1 and 3-2 in the Supporting Information.

Isomerization Equilibrium. The analysis of the isomerization equilibrium was performed in the C−Br stretch-band region. The areas of the bands were determined after background subtraction either by integrating the bands to the left and right side of the minimum between the two bands or from the ratio of the areas of Gaussian or Voigt functions independently fit the two bands, avoiding the region in which they overlap. For both free and mixed (bound + free) 1-BP, seven spectra from independent experiments were obtained and the bands were analyzed using the above area estimation methods. The reported area ratios for free and bound 1-BP correspond to the average and standard deviation of a set of 21 area ratios that were obtained for each system at 20 °C. For pure liquid 1-BP, four independent spectra were collected and analyzed in the same way. The spectrum of the bound 1-BP species in the solid crystal was obtained from the difference between the spectra of α-CD-1-BP crystal and α-CD powder (see the Supporting Information and Figure S1 for more information). Unpolarized Raman spectra were collected from four different orientations/regions of the solid samples, with no attempt to orient the crystals, and the

corresponding bound 1-BP spectra were used to obtain the corresponding *gauche-trans* area ratios of 1-BP bound in α-CD.

3.3 Results and Discussion

Figure 3-1 shows the measured Raman spectra of water, a 20 mmol L^{-1} solution of α-CD, and saturated solutions of 1-BP in water and in 20 mmol L^{-1} aqueous α-CD at 20 °C. Note that 1-BP was maintained at its saturation concentration by immersing a droplet of liquid 1-BP in the corresponding aqueous solutions. All Raman spectra shown in Figure 3-1 (a) look very similar to those of pure water except for a small shoulder on the left side of the O−H stretching band due primarily to the C−H stretch of α-CD. The resulting Raman-MCR SC spectra shown in Figure 3-1 (b) are more revealing, as they uncover multiple intramolecular vibrational bands of both α-CD and 1-BP. Specifically, the red curve represents the SC spectrum of unbound 1-BP, the purple curve corresponds to the SC spectrum of a mixture of bound and unbound 1-BP, and the green curve is the SC spectrum of α-CD in water. The latter α-CD spectral features are not present in the bound 1-BP spectrum, as they were effectively subtracted away by the SMCR spectral decomposition process in which the solution contains both 1-BP and α-CD and the solvent contains only α-CD, both with the same α-CD concentration of ∼20 mmol L^{-1}. The increase, by nearly a factor of 2, of the 1-BP band intensities in the presence of α-CD (compare the purple and red spectra) clearly reveals that the α-CD binding induced an increase in the solubility of 1-BP. Note that this factor of 2 is a lower bound to the actual binding-induced solubilization of 1-BP, as both our experimental and theoretical results indicated that the Raman cross section of bound 1-BP is smaller than that of 1-BP dissolved in water (see the Supporting Information for further details).

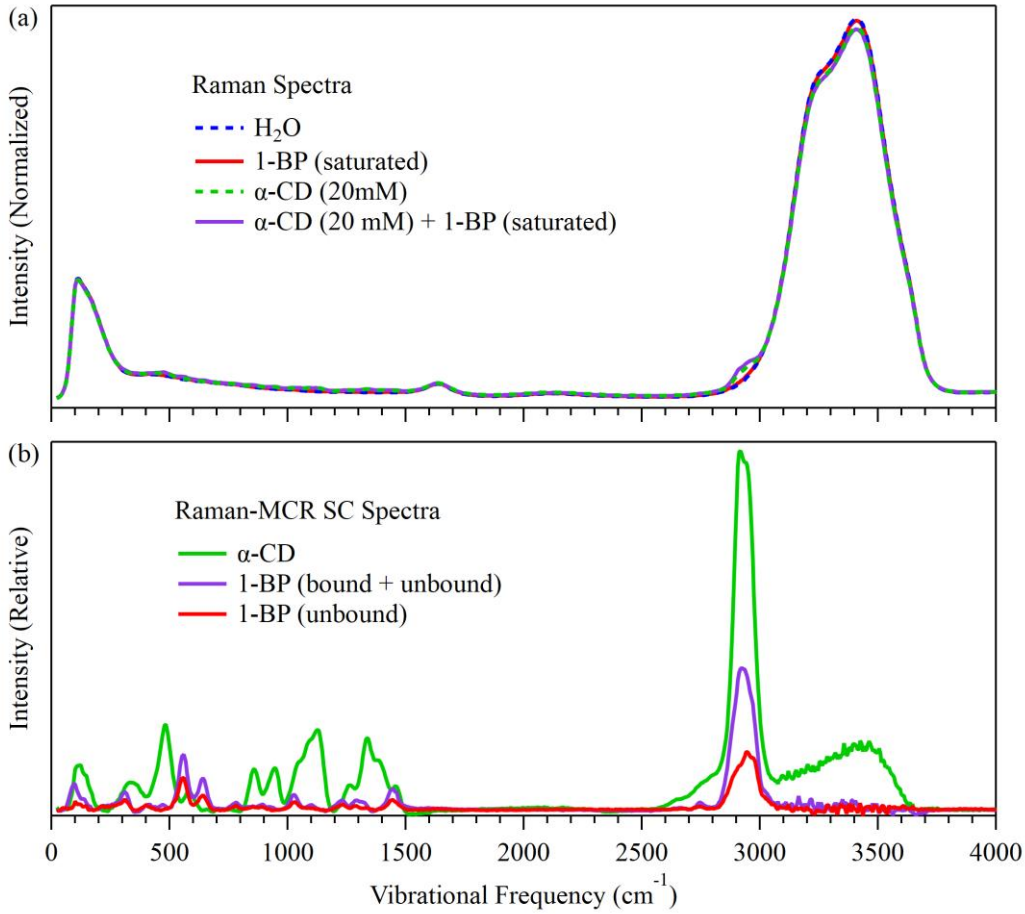

Figure 3-1. Raman spectra in (a), all normalized to the same area, are used to obtain the Raman-MCR SC spectra in (b) for unbound aqueous α-CD (green) and 1-BP (red), as well as an equilibrium mixture (purple) of free and bound 1-BP in a 20 mM α-CD solution saturated with 1-BP.

Figure 3-2 shows an expanded view of the C−Br stretch bands for the two conformers of 1-BP in a saturated aqueous solution (red) and in a solution containing 20 mmol L^{-1} α-CD (purple), along with the associated fits to a superposition of two Gaussians. The assignment of these peaks to the *gauche* (at ~560 cm^{-1}) and *trans* (at ~650 cm^{-1}) isomers are confirmed both by the disappearance of the *gauche* peak upon freezing pure 1-BP,[30] as well as our own (and prior)[31] quantum calculations (see the Methods section and Supporting Information). The associated *gauche* and *trans* band areas, A_G and A_T, may be obtained either by directly integrating the experimental spectra to the left and right of the minimum between the two bands or from the areas of the corresponding Gaussian (or Voigt) fits to the experimental bands, and the resulting band area ratios agree to within ~5 %. All of the reported equilibrium constant (K_{eq}) values are average

values obtained using three different area measurement methods (see the Methods section for further details). The band area of each conformer may be expressed as $A_i = c_i\sigma_i$, where c_i and σ_i are the concentration and Raman scattering cross section of the ith conformer, respectively. Therefore, the equilibrium constant is $K_{eq} = c_G/c_T = (A_G/\sigma_G)/(A_T/\sigma_T)$. Importantly, quantum calculations indicate that the two conformers have approximately the same C−Br Raman cross section ratio, $\sigma_G/\sigma_T \sim 1$, both in the gas phase and in a dielectric implicit aqueous solvent, and thus the ratio of the band areas provides a spectroscopic measure of K_{eq} (see the Methods section and Supporting Information for additional details). However, our quantum calculations also indicate that the C−Br Raman cross sections decrease upon binding and have a significantly different ratio of $\sigma_G/\sigma_T \sim 3$, thus also influencing the measured isomerization free energy and entropy, as further discussed below. It is also noteworthy that the influence of host-guest binding on molecular polarizabilities and optical spectra have previously been described[32] but not, to our knowledge, with regard to Raman cross sections or the associated changes in polarizability with respect to the corresponding vibrational and conformational degrees of freedom.

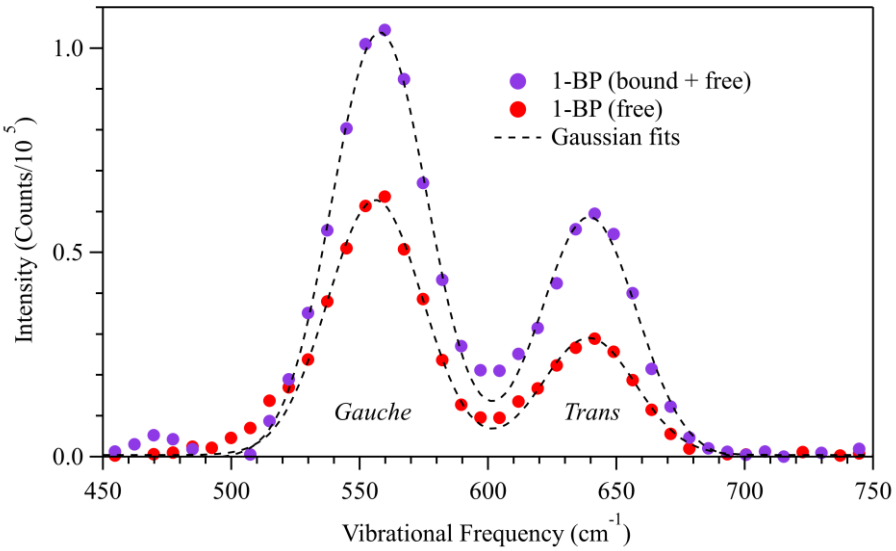

Figure 3-2. Raman-MCR SC spectra in the C−Br stretch region. The points are the experimental intensities, and the dashed curves are the sum of Gaussian fits to the two sub-bands.

If we assume that binding does not change the Raman scattering cross section ratio, $\sigma_G/\sigma_T \sim 1$, then the isomerization equilibrium constant for the 1-BP bound to α-CD, obtained from the difference between the purple and red band areas in Figure 3-2, implies that $K_{eq} \sim 1.4 \pm 0.3$, which

is nearly a factor of 2 smaller than that of 1-BP dissolved in water, K_{eq} ~2.3 ± 0.2. However, our DFT calculations of the 1-BP isomers bound in α-CD indicate that the Raman scattering cross section of the bound *gauche* conformer is three times larger than the bound *trans* conformer and thus σ_G/σ_T ~3 (see the Methods section and Supporting Information for additional details). If we use this predicted cross section ratio, then the inferred conformational equilibrium constant further decreases to K_{eq} ~0.5 ± 0.2 in the bound host-guest complex. In either case, the decrease in K_{eq} upon transfer from the aqueous solution to the α-CD cavity implies that the 1-BP conformation equilibrium shifts toward the *trans* conformer upon binding to α-CD. Moreover, our additional Raman measurements of the solid complex imply that the conformation equilibrium constant is approximately the same in the solid state as it is for the complex dissolved in liquid water (as further described below).

Figure 3-3 compares C−Br stretch bands of 1-BP in the pure liquid (a), aqueous solution (b), and bound in α-CD in the aqueous (c) and solid (d) complexes, along with the corresponding partial molar Gibbs free-energy change $\Delta G = -RT \ln K_{eq}$ for the *trans* to *gauche* isomerization process. The ΔG values shown in panels (a,b) are within ± 0.2 kJ mol^{-1} of previously reported Raman-based experimental results in pure liquid[33,34] and aqueous[35] 1-BP. The bound 1-BP spectra in panels (c,d) were obtained from the difference between the bound and unbound spectra assuming σ_G/σ_T ~3 (as explained above, with further details provided in the Methods section and Supporting Information). Note that the negative-going feature in panel (c) is a subtraction artifact resulting from the large α-CD peak near 480 cm^{-1} (see Figure 3-1). Fine-tuning the subtraction to minimize this artifact does not significantly alter the resulting K_{eq} (and ΔG).

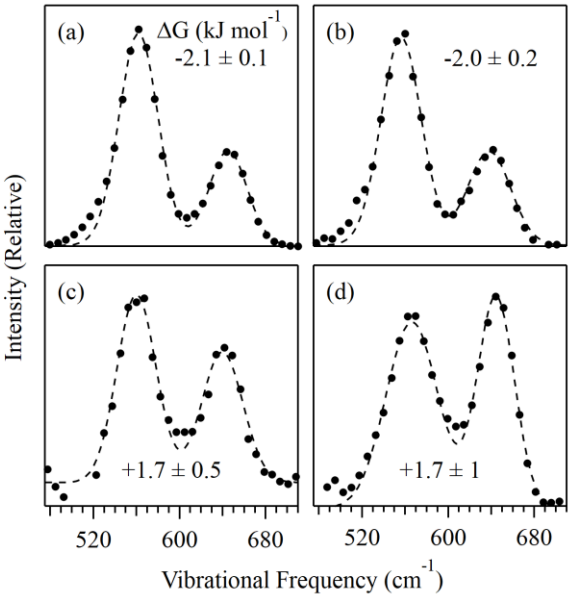

Figure 3-3. Raman spectra (and Gaussian fits) of the 1-BP C−Br stretch bands obtained for different systems and the corresponding free energy $\Delta G = -RT \ln K_{eq}$ at 293.15 K. (a) Pure liquid 1-BP ($K_{eq} \sim 2.4 \pm 0.1$), (b) aqueous 1-BP ($K_{eq} \sim 2.3 \pm 0.2$), (c) 1-BP bound to α-CD in the aqueous solution ($K_{eq} \sim 0.5 \pm 0.2$) and (d) in the solid crystal ($K_{eq} \sim 0.5 \pm 0.1$). Note that the above ΔG values in (c,d) were obtained assuming $\sigma_G/\sigma_T \sim 3$ (as discussed in the text).

To gain further insight into the distribution of *gauche* and *trans* isomers inside the α-CD molecules, we also analyzed crystalline samples of the host-guest complex using single-crystal X-ray diffraction. The overall packing and arrangement of the constituent entities in the crystal structure are dominated by the α-CD molecules connected to each other through a hydrogen-bonding network between the hydroxyl moieties of neighboring molecules creating a dense packing that leaves no open space other than the interior of the cylindrical α-CD molecules. The observed structures differ from that of native α-CD but are closely related to a series of other guest hosting α-CD complexes. A search of the Cambridge structural database[36] revealed several α-CD host-guest complexes with acetone,[37] thiophene,[38] diethylfumarate,[39] hemikis(2,2′-azodipyridine),[40] n-butylisothiocyanate,[41] lithium triiodide iodine,[42] and various metallocene complexes having unit cell shapes and α-CD packing that differ from the α-CD-1-BP complex only by the nature of the guests in the cavity. Both α-CD-1-BP and its isomorphous counter parts are characterized by a stacking arrangement of α-CD molecules with the unit cell having two α-CD molecules forming a head-to-head dimer (capsule). Molecules line up in such a

way that the interior voids of the cylindrical α-CD molecules connect to form channels extending through the crystal along the c-axis of the unit cell (Figure 3-4).

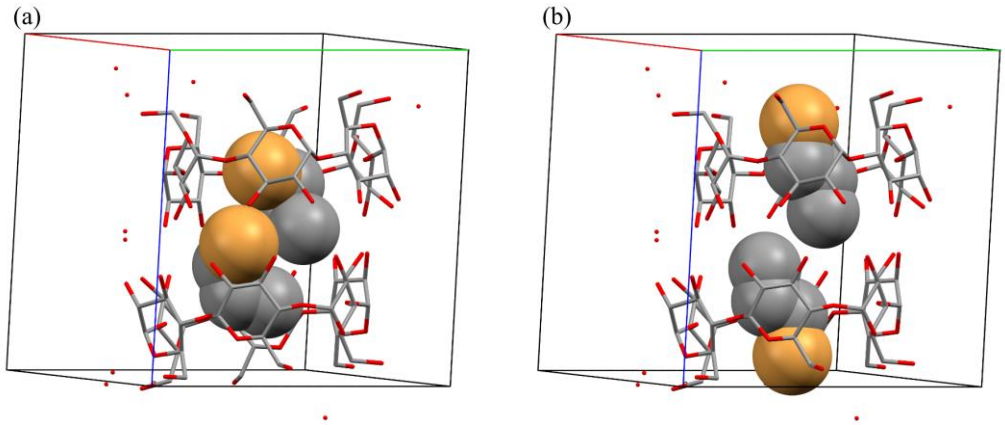

Figure 3-4. (a) View of the α-CD-1-BP dimer showing the most probable gauche configurations [10.4(2) and 17.5(2) %]. (b) View of the α-CD-1-BP dimer showing the most probable trans configurations [28.8(4) and 51.5(4) %]. The red, green, and blue lines point along the a, b and c axes, respectively (see the SI for further details).

Single-crystal X-ray diffraction provides an average of the arrangement of all constituent entities over the entire crystal (in the form of the electron densities inside the crystallographic repeat units, the unit cell). If positions of atoms or fragments differ between unit cells, then disorder has to be included when building the structural model based on the diffraction data. Two different types of disorder are observed in the structure: (1) the two-fold disorder of a water molecule, inducing disorder of two of twelve crystallographically independent α-CD sugar moieties (see the Supporting Information for details regarding this disorder) and (2) the disorder associated with the two conformations of 1-BP embedded in the cavities of the two α-CD molecules in each unit cell, as described in greater detail below (and in the Supporting Information).

Figure 3-4 shows representative unit cell structures obtained from the α-CD-1-BP single-crystal X-ray diffraction analysis. Figure 3-4 (a) shows the most probable bound *gauche* conformers, while Figure 3-4 (b) shows the most probable bound *trans* conformers. Note that although (a) has two *gauche* and (b) has two *trans* 1-BP molecules, the X-ray results do not imply that the structures are invariably paired in this way. In other words, the X-ray structures are equally

consistent with unit cell structures in which neighboring α-CD hosts contain different 1-BP conformers.

More specifically, the single-crystal data indicate that in the crystal, each α-CD molecule contains exactly one bound 1-BP molecule disordered over several slightly shifted and rotated positions of both the *trans* and *gauche* conformations. Major moiety disordered molecules as well as their assignment as *gauche* or *trans* were immediately evident from difference electron density maps and were assigned and modeled. This was followed by re-analysis of difference density maps and assignment of successively less prevalent disordered moieties until the remaining difference electron density maps were essentially featureless. In total, six conformations were modeled for each of the 1-BP molecule in the two-independent α-CD molecules with refined occupancies between 0.515(4) and 0.0561(19). All 1-BP molecules are clearly associated with one of the two α-CD molecules, with no 1-BP molecules stretching along the channel between the two α-CD hosts. Total occupancies for all disordered moieties refined to close to unity for each site, indicating the absence of empty or water filled α-CD cavities. In the final refinement cycle, the total occupancy was constrained to exactly one. In the crystal structure, measured at 150 K, the trans conformation is significantly favored (as further discussed below). After applying structural restraints to the 1-BP molecules embedded inside the α-CD dimer (see the Supporting Information for details), the 1-BP molecules in the two α-CD structures had *gauche-trans* ratios of 0.26/0.74 and 0.35/0.65 at 150 K, giving an average K_{eq} ~0.3/0.7 ~0.4 ± 0.1 (with error bars obtained from the ± 0.05 difference between the individual conformer probabilities in the first and second crystallographically distinct structures). This slightly smaller value of K_{eq} at 150 K, relative to the K_{eq} ~0.5 for the bound complex at 293 K, is consistent with positive ΔH for the *trans* to *gauche* conformation change in the α-CD host. The positive sign of ΔH is also consistent with the following temperature dependent Raman measurements of the conformer peak ratio in the solid complex.

Figure 3-5 shows results obtained from temperature-dependent measurements of the 1-BP *trans* to *gauche* (folding) equilibrium constant to obtain the corresponding isomerization ΔH and ΔS values. Specifically, the *trans* to *gauche* enthalpy and entropy changes are obtained from the corresponding temperature-dependent ΔG values using $\Delta H = [\partial(\Delta G/T)/\partial(1/T)]_P$ and $\Delta S = (\partial \Delta G/\partial T)_P$. The error associated with such temperature-dependent measurements correspond

to uncertainties of ±1−2 kJ mol^{-1} in ΔH and ±2−6 J K^{-1} mol^{-1} in ΔS (with an additional uncertainty in ΔS resulting from the Raman cross section ratio, as further discussed below).

In spite of the significant uncertainties associated with the isomerization enthalpy, the ΔH of ~0.1 kJ mol^{-1} for 1-BP in the pure liquid is within the range of the previously reported values, varying between 0.1 kJ mol^{-1} < ΔH < 1.1 kJ mol^{-1}.[43-45] More interestingly, our results indicate that the *trans* to *gauche* ΔH changes sign upon binding to α-CD. Specifically, ΔH is negative for 1-BP dissolved in water but becomes positive upon binding to α-CD, while the sign ΔS changes from positive to negative upon binding. This implies that the *trans* conformer has both an enthalpically and entropically more favorable interaction with the α-CD cavity. The conformational ΔS change is more difficult to accurately quantify than ΔH both because of its small magnitude (relative to the error bars of the associated data points) and because, unlike ΔH, the value of the experimentally inferred ΔS is sensitive to binding-induced changes in the relative Raman cross section of the two conformers. Note that the unbound ΔS values in Figure 3-5 (b,d) are positive and, within experimental error, have the same magnitude as $\Delta S = R \ln 2 \approx 6$ J K^{-1} mol^{-1} obtained assuming that the entropy changes are entirely due to the fact that there are two *gauche* conformers and only one *trans* conformer.[23,46]

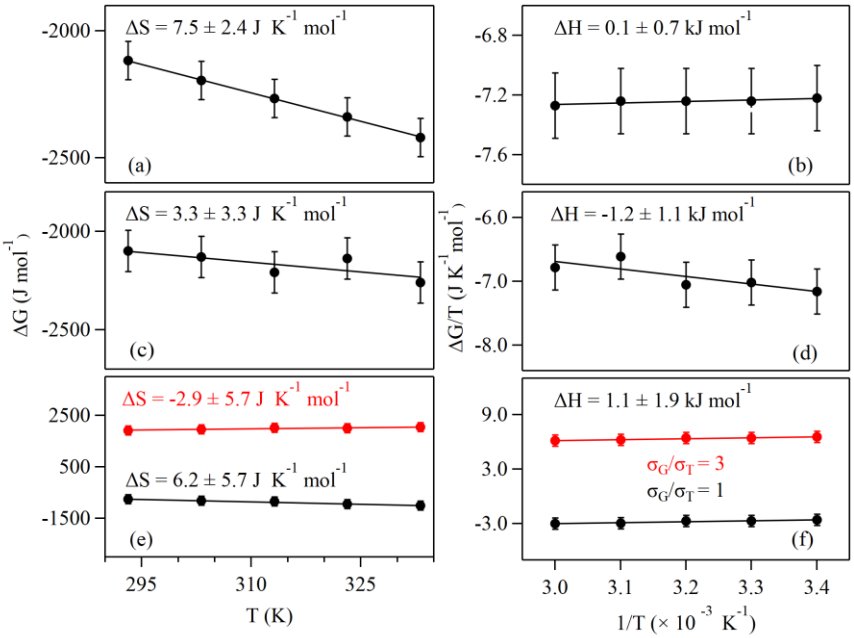

Figure 3-5. Experimental isomerization (*trans* to *gauche*) entropy and enthalpy for 1-BP for pure liquid 1-BP (a,b), aqueous 1-BP (c,d), and α-CD-1-BP complex in the crystalline solid state (e,f). Note that the $-T\Delta S$ entropic contributions to ΔG at 293.15 K range from -2.2 ± 0.7 kJ mol^{-1} in the pure 1-BP liquid to -1.0 ± 1.0 kJ mol^{-1} in the aqueous solution. In the case of bound 1-BP, at 293.15 K, the entropic contribution is -1.8 ± 1.7 kJ mol^{-1}, assuming σ_G/σ_T ~1 or 0.9 ± 1.8 kJ mol^{-1}, assuming σ_G/σ_T ~3.

Deviations from this value may arise from various sources, including differences between the internal partition functions of the two isomers, as well as the surrounding host and/or solvent molecules. However, the bound ΔS value in Figure 3-5 (f), obtained assuming that σ_G/σ_T ~3, has the opposite sign, implying that the bound *trans* conformer has more thermally accessible configurations than the *gauche* conformation. Thus, the binding-induced sign change of ΔS is consistent with a looser fit of the *trans* conformer to the α-CD cavity, while the sign change of ΔH implies that the tighter fit of the *gauche* conformer to α-CD cavity has a greater repulsive interaction with the cavity walls.

It is also noteworthy that ΔG ~1.1 ± 0.3 kJ mol^{-1} for the folding of 1-BP in α-CD at 150 K, obtained directly from the X-ray crystal diffraction analysis, is roughly consistent with the value of ΔG ~1.5 ± 6.0 kJ mol^{-1} obtained from ΔS ~-2.9 J K^{-1} mol^{-1} (assuming σ_G/σ_T ~3) and ΔH ~1.1 kJ mol^{-1}, when extrapolated down to 150 K. The approximate agreement between the latter two ΔG values for bound 1-BP at 150 K implies that ΔS and ΔH remain approximately

temperature independent between 150 and 335 K and provides additional support for the prediction that σ_G/σ_T ~3 for 1-BP bound within the α-CD cavity.

3.4 Conclusions

In summary, Raman-MCR and X-ray crystallographic measurements reveal that 1-BP remains flexible upon binding to α-CD, although its conformation equilibrium is shifted toward the unfolded trans conformation upon binding. Our experimental temperature-dependent Raman measurements on both free and α-CD-bound 1-BP, combined with our predicted binding-induced Raman cross section changes, imply that both the conformational enthalpy and entropy of 1-BP change sign upon binding to α-CD. The latter sign changes, as well as the corresponding conformational free energy, are all consistent with a more favorable fit of the *trans* conformer to the α-CD cavity.

3.5 Supplementary Information

Raman spectra of the solid α-CD-1-BP crystal. Figure 3-6 shows the Raman spectra collated for both solid α-CD (orange dots) and a crystal of the α-CD-1-BP complex (blue dots). Note that α-CD has a peak that overlaps primarily with the C−Br stretch band of the *gauche* 1-BP conformer. After normalizing both spectra to the α-CD peak at ~485 cm^{-1}, the difference spectrum (black dots) between the blue and orange spectra was obtained. The black-dashed curve is the sum of Gaussian fits to the non-overlapping portions of the *gauche* and *trans* peaks. This difference spectrum is that arising from the 1-BP molecules that are bound to α-CD in the crystal. Similar results were obtained from four different (randomly oriented) crystals.

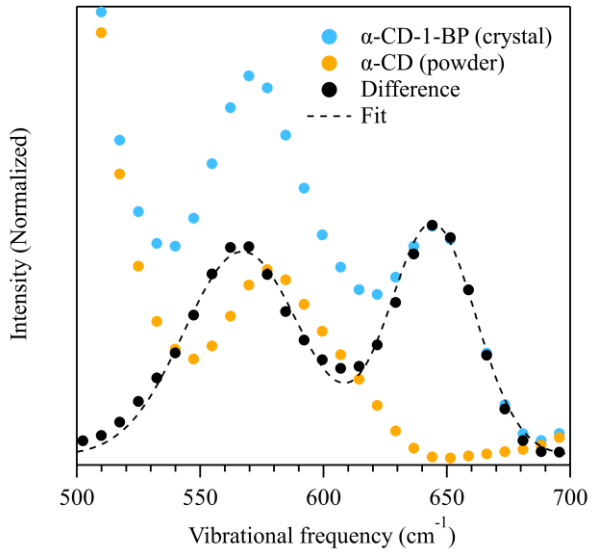

Figure 3-6. Generation of difference spectrum corresponding to bound 1-BP species present in the crystal.

Predicted *gauche-trans* Raman cross-section ratios. Tables 3-1 and 3-2 contain calculated Raman activities and Raman cross sections, respectively, for 1-BP obtained as described in the Methods section. The Raman cross sections (σ) were calculated from Raman activity using equation 42 in the paper by Neugebauer and coworkers.[47]

Table 3-1. Frequencies and Raman activities calculated at two levels of theory for different 1-BP systems.

Level of theory	1-BP systems	C-Br stretch mode	Frequency (cm^{-1})	Raman Activity ($Å^4$/AMU)
B3LYP/6-31g(dp)	-	*G*	557.64	15.69
		T	645.40	18.42
	Water (CPCM)	*G*	540.32	38.81
		T	625.44	47.48
	α-CD	*G*	564.29	15.28
		T	638.33	6.17
WB97/LANL2DZ	-	*G*	587.15	23.06
		T	676.45	26.08
	Water (CPCM)	*G*	565.48	55.70
		T	654.49	63.31
	α-CD	*G*	588.62	23.53
		T	660.66	8.79

Table 3-2. *Gauche-trans* Raman cross-section ratio (σ_G/σ_T) predicted at two levels of theory.

Level of theory	1-BP systems	σ_G/σ_T
B3LYP/6-31g(dp)	-	1.1
	Water (CPCM)	1.0
	α-CD	3.0
WB97/LANL2DZ	-	1.1
	Water (CPCM)	1.1
	α-CD	3.2

Binding-induced C-Br Raman cross-section changes. In order to corroborate experimentally the changes in the Raman cross section of the bound 1-BP conformers, a small amount (6 mg) of α-CD was added to an aqueous 1-BP solution with a known concentration of 10 mM. The Raman spectra of these solutions as well as the Raman spectrum of an aqueous α-CD solution (3 mM) and water were collected and treated using SMCR. Figure 3-7 compares the SC spectrum of unbound 1-BP with the SC spectrum of a mixture of bound and unbound 1-BP. Notice that upon binding the cross-sections of the C−Br stretching modes of both conformers decrease, as the total area of the two C−Br stretch bands is ~27% smaller in the aqueous α-CD solution than it is in pure water. Moreover, this change does not occur equally in the two peaks, as the *gauche* and *trans* peak areas decrease by ~30% and ~20%, respectively, which is consistent with a shift of the 1-BP equilibrium

towards the *trans* conformation (particularly since the Raman cross section of the trans C−Br band is predicted to have a great binding-induced Raman cross section decrease).

If it is assumed that, under the above conditions, all the α-CD cavities are occupied by a single 1-BP guest, and thus 30% of all the 1-BP molecules are bound in α-CD (and the remainder are dissolved in water), then that would imply that the Raman cross section of bound 1-BP is approximately 10 times smaller than that of free 1-BP dissolved in water. The latter binding induced decrease slightly larger, but of comparable magnitude, to the predicted 2-to-7-fold decrease, obtained by comparing the predicted Raman cross section of the 1-BP *gauche* and *trans* conformers in water and in α-CD (see Table 3-2).

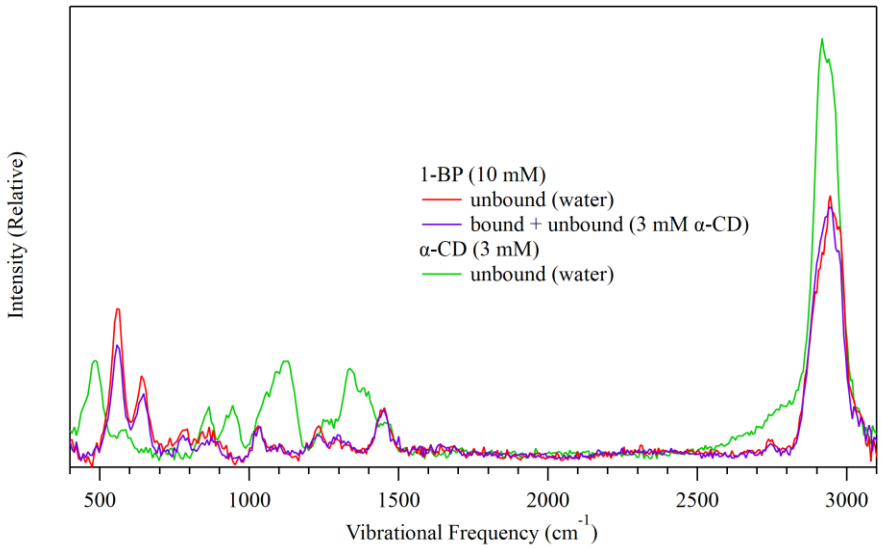

Figure 3-7. Raman cross-section change of the C−Br stretching mode of both the *gauche* and *trans* conformers upon binding to α-CD.

Gas Phase 1-BP Raman Spectra and Thermodynamics. The Raman spectra shown in Fig. 3-8 were obtained from the vapor above the pure liquid in a closed glass vial mounted in a variable temperature cell holder. The temperature dependent increase in the area of the C−Br stretch bands reflects the corresponding increase in vapor pressure.

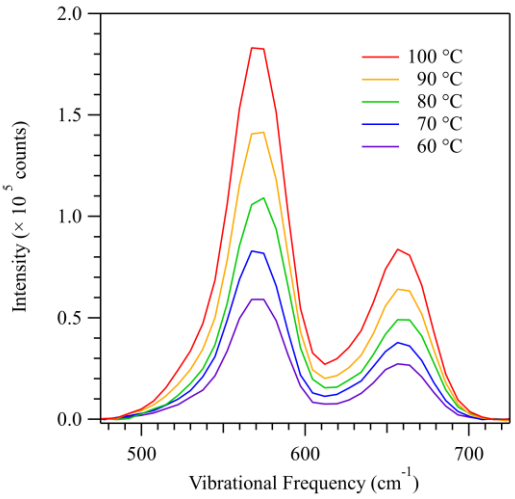

Figure 3-8. Raman spectra of gaseous 1-BP in the C−Br stretch region at different temperatures, obtained after subtraction of the Raman spectra of the glass vial taken under the same conditions.

The temperature dependence of the vapor pressure of 1-BP can be calculated using the Antoine equation: $\log_{10} P = A\text{-}B/(T+C)$, using previously tabulated coefficients (A, B, and C).[48] Figure 3-9 shows a good correlation between vapor pressures and the C−Br band areas thus confirming the proportionality between the measured Raman intensity and vapor pressure.

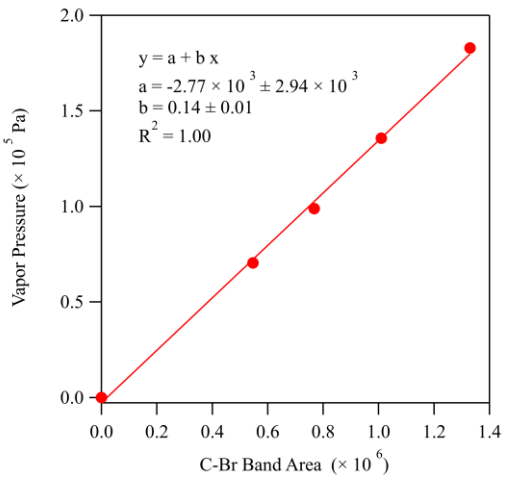

Figure 3-9. Vapor pressure vs. area of the C−Br bands in Figure 3-8.

Figures S5 and S6 show the temperature dependent measurements of the 1-BP *gauche*/*trans* equilibrium constant (obtained assuming $\sigma_G/\sigma_T \sim 1$), and the resulting ΔG, ΔS, and ΔH. Although the ΔS results are quite noisy, they imply that ΔS has the same sign as that in the pure liquid and

aqueous solution and is within error bars of the latter ΔS value. The ΔH in the gas phase also has the same sign and comparable magnitude to that in the pure liquid and aqueous solutions. This confirms that the stabilization of the *gauche* conformers in the liquid state is primarily due to an intramolecular interaction, such as the van der Waals attraction of the terminal methyl and Br groups, referred to as the "*gauche* effect".

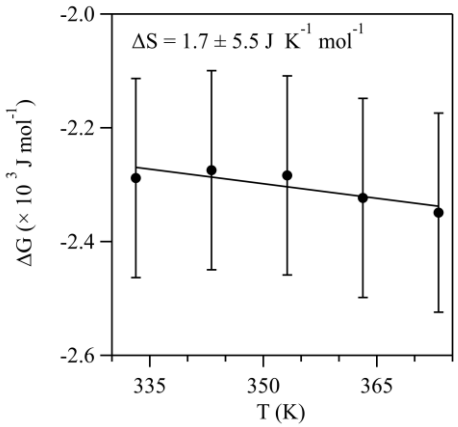

Figure 3-10. Experimental isomerization (*trans* to *gauche*) entropy for gaseous 1-BP.

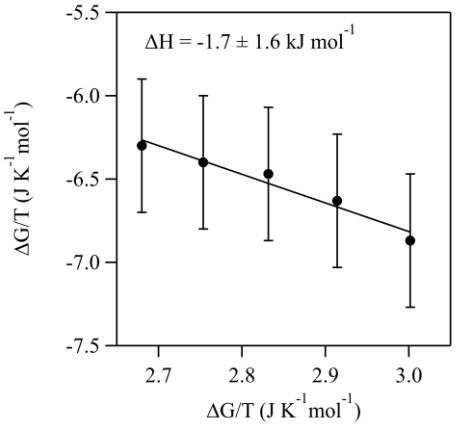

Figure 3-11. Experimental isomerization (*trans* to *gauche*) enthalpy for gaseous 1-BP.

Single Crystal X-ray Diffraction. Data were collected, reflections were indexed and processed, and the files scaled and corrected for absorption using APEX3[49] and SADABS[50]. The space group was assigned, and the structure was solved by direct methods using XPREP within the SHELXTL suite of programs[51] and refined by full matrix least squares against F^2 with all reflections using Shelxl2018[52] using the graphical interface Shelxle[53]. H atoms attached to carbon and hydroxyl

hydrogens were positioned geometrically and constrained to ride on their parent atoms. C-H bond distances were constrained to 1.00, 0.99 and 0.98 Å for aliphatic C-H, CH_2 and CH_3 moieties, respectively. α-CD O-H distances of alcohols were constrained to 0.84 Å. Methyl CH_3 and hydroxyl H atoms were allowed to rotate but not to tip to best fit the experimental electron density. Water H atom positions were refined, and O-H distances were restrained to 0.84(2) Å. Where necessary, water H···H distances were restrained to 1.36(2) Å, and H atom positions were further restrained based on hydrogen bonding considerations. Isotropic displacement parameters of hydrogen atoms U_{iso}(H) were set to a multiple of the equivalent isotropic displacement parameters of the U_{eq}(C) of the anisotropic displacement parameters, with 1.5 for CH_3 and OH, and 1.2 for C-H and CH_2 units, respectively.

The structure features two crystallographically independent α-CD molecules that each consist of six dextrin moieties linked end to end via α-1, 4 linkages. A common atom naming scheme was used for all dextrin moieties, with each moiety uniquely identified by atom label suffixes: A-F for molecule 1, and G-L for moiety 2. Two different types of disorder are observed in the structure. Disorder of a water molecule, inducing disorder of the surrounding α-CD sugar moieties. And disorder of 1-BP molecules embedded in the cavity of the two crystallographically independent α-CD molecules. The water-α-CD disorder involves parts of sugar moieties E and G. The major and minor E and G moieties were each restrained to have similar geometries using SAME and SADI commands of Shexl2018. U^{ij} components of anisotropic displacement parameters (ADPs) for disordered atoms closer to each other than 2.0 Å were restrained to be similar (applied estimated standard deviation, esd, 0.01 $Å^2$). Atoms O5E1 and O5E2 as well as O4E1 and O4E2 were each constrained to have identical ADPs. Subject to these conditions the occupancy ratio refined to 0.606(5) to 0.394(5).

Each of the two α-CD molecules houses one 1-BP molecule, disordered over several slightly shifted and rotated positions, with both *trans* and *gauche* conformations observed. Major moiety disordered molecules as well as their assignment as *gauche* or *trans* were immediately evident from difference density maps and were assigned and modeled, followed by re-analysis of difference density maps and assignment of successively less prevalent disordered moieties, until the remaining difference density maps were essentially featureless. Total occupancies for all disordered moieties refined to close to unity for each site and were constrained to exactly one in the final refinement cycles. Equivalent bond distances and angles, but not torsion angles, of all

1-BP moieties were restrained to be similar (SAME restraint of Shelxl, applied esd 0.02 Å). U^{ij} components of ADPs for 1-BP atoms closer to each other than 2.0 Å were restrained to be similar (applied esd 0.01 $Å^2$). The atom C32 of one 1-BP moiety was restrained from approaching the α-CD moiety too closely (DFIX -3.0 command of Shelx2018). Subject to these conditions the occupancy rates refined to the following:

Embedded inside molecule 1 (sugar moieties A through F):
Br1 (*trans*) 0.288(4)
Br4 (*gauche*) 0.0833(17)
Br5 (*gauche*) 0.0723(18)
Br7 (*trans*) 0.167(4)
Br8 (*trans*) 0.285(4)
Br10 (*gauche*) 0.104(2)
Total *trans* to *gauche* ratio: 0.74:0.26

Embedded inside molecule 2 (sugar moieties G through L):
Br2 (*trans*) 0.515(4)
Br3 (*gauche*) 0.1750(18)
Br6 (*trans*) 0.133(3)
Br9 (*gauche*) 0.121(4)
Br11 (*gauche*) 0.0561(19)
Total *trans* to *gauche* ratio: 0.65:0.35

Additional details are given in Table 3-3. Complete crystallographic data, in CIF format, have been deposited with the Cambridge Crystallographic Data Centre. CCDC contains the supplementary crystallographic data for this paper. These data can be obtained free of charge from the Cambridge Crystallographic Data Centre via www.ccdc.cam.ac.uk/data_request/cif (CCDC 2023037).

Table 3-3. Details of the single crystal X-Ray diffraction experiment.

	VB_1_exp1_0m
Crystal data	
Chemical formula	$2(C_{36}H_{60}O_{30})\cdot 2(C_3H_7Br)\cdot 9(H_2O)$
M_r	2353.81
Crystal system, space group	Triclinic, *P*1
Temperature (K)	150
a, *b*, *c* (Å)	13.7626 (6), 13.8666 (6), 15.6527 (7)
α, β, γ (°)	93.104 (2), 91.6464 (19), 119.3788 (15)
V (Å^3)	2593.9 (2)
Z	1
F(000)	1242
D_x (Mg m^{-3})	1.507
Radiation type	Mo *K*α
No. of reflections for cell measurement	9473
θ range (°) for cell measurement	2.2–35.7
μ (mm^{-1})	0.90
Crystal shape	Fragment
Colour	Colourless
Crystal size (mm)	0.43 × 0.42 × 0.23
Data collection	
Diffractometer	Bruker AXS D8 Quest CMOS diffractometer
Radiation source	sealed tube X-ray source
Monochromator	Triumph curved graphite crystal
Scan method	ω and phi scans
Absorption correction	Multi-scan, *SADABS* 2016/2: Krause, L., Herbst-Irmer, R., Sheldrick G.M. & Stalke D., J. Appl. Cryst. 48 (2015) 3-10
T_{min}, T_{max}	0.665, 0.747
No. of measured, independent and observed [$I > 2\sigma(I)$] reflections	146000, 48981, 37919
R_{int}	0.040
θ values (°)	θ_{max} = 36.5, θ_{min} = 2.9
$(\sin\theta/\lambda)_{max}$ (Å^{-1})	0.837
Range of *h*, *k*, *l*	*h* = -22→22, *k* = -23→23, *l* = -26→26

Table 3-3 continued	
Refinement	
Refinement on	F^2
$R[F^2 > 2\sigma(F^2)]$, $wR(F^2)$, S	0.045, 0.127, 1.03
No. of reflections	48981
No. of parameters	1896
No. of restraints	2031
H-atom treatment	H atoms treated by a mixture of independent and constrained refinement
Weighting scheme	$w = 1/[\sigma^2(F_o^2) + (0.0717P)^2]$ where $P = (F_o^2 + 2F_c^2)/3$
$(\Delta/\sigma)_{max}$	0.006
$\Delta\rho_{max}$, $\Delta\rho_{min}$ (e Å^{-3})	0.65, -0.48
Extinction method	*SHELXL2018*/3 (Sheldrick 2018), $Fc^*=kFc[1+0.001xFc^2\lambda^3/\sin(2\theta)]^{-1/4}$
Extinction coefficient	0.0106 (12)
Absolute structure	Flack x determined using 15366 quotients [(I+)-(I-)]/[(I+)+(I-)] (Parsons, Flack and Wagner, Acta Cryst. B69 (2013) 249-259).
Absolute structure parameter	0.018 (2)

Computer programs: Apex3 v2017.3-0 (Bruker, 2016), SAINT V8.38A (Bruker, 2016), SHELXS97 (Sheldrick, 2008), SHELXL2018/3 (Sheldrick, 2015, 2018), SHELXLE Rev924 (Hübschle et al., 2011).

3.6 References

(1) Koshland, D. E. Conformational changes: How small is big enough? *Nat. Med.* **1998**, 4, 1112.

(2) Mesecar, A. D.; Stoddard, B. L.; Koshland, D. E. Orbital steering in the catalytic power of enzymes: Small structural changes with large catalytic consequences. *Science* **1997**, 277, 202.

(3) Ahmad, E.; Rabbani, G.; Zaidi, N.; Khan, M. A.; Qadeer, A.; Ishtikhar, M.; Singh, S.; Khan, R. H. Revisiting ligand-induced conformational changes in proteins: Essence, advancements, implications and future challenges. *J. Biomol. Struct. Dyn.* **2013**, 31, 630.

(4) Ahmad, M.; Helms, V.; Kalinina, O. V.; Lengauer, T. The role of conformational changes in molecular recognition. *J. Phys. Chem. B* **2016**, 120, 2138.

(5) Chiarparin, E.; Packer, M. J.; Wilson, D. M. Experimental free ligand conformations: A missing link in structure-based drug discovery. *Future Med. Chem.* **2019**, 11, 79.

(6) van Zundert, G. C. P.; Hudson, B. M.; de Oliveira, S. H. P.; Keedy, D. A.; Fonseca, R.; Heliou, A.; Suresh, P.; Borrelli, K.; Day, T.; Fraser, J. S.; van den Bedem, H. Qfit-ligand reveals widespread conformational heterogeneity of drug-like molecules in x-ray electron density maps. *J. Med. Chem.* **2018**, 61, 11183.

(7) Mobley, D. L.; Dill, K. A. Binding of small-molecule ligands to proteins: "What you see" is not always "what you get". *Structure* **2009**, 17, 489.

(8) Sasmal, S.; Gill, S. C.; Lim, N. M.; Mobley, D. L. Sampling conformational changes of bound ligands using nonequilibrium candidate monte carlo and molecular dynamics. *J. Chem. Theory Comput.* **2020**, 16, 1854.

(9) Gibb, C. L. D.; Gibb, B. C. Straight-chain alkanes template the assembly of water-soluble nano-capsules. *Chem. Commun.* **2007**, 1635.

(10) Scarso, A.; Trembleau, L.; Rebek, J. Helical folding of alkanes in a self-assembled, cylindrical capsule. *J. Am. Chem. Soc*. **2004**, 126, 13512.

(11) Velpuri, S. V. V.; Gade, H. M.; Wanjari, P. P. Encapsulation driven conformational changes in n-alkanes inside a hydrogen-bonded supramolecular cavitand assembly. *Chem. Phys*. **2019**, 521, 100.

(12) Wanjari, P. P.; Sangwai, A. V.; Ashbaugh, H. S. Confinement induced conformational changes in n-alkanes sequestered within a narrow carbon nanotube. *Phys. Chem. Chem. Phys.* **2012**, 14, 2702.

(13) Rebek, J. Molecular behavior in small spaces. *Acc. Chem. Res.* **2009**, 42, 1660.

(14) Davis, M. E.; Brewster, M. E. Cyclodextrin-based pharmaceutics: Past, present and future. *Nat. Rev. Drug Discovery* **2004**, 3, 1023.

(15) Kolesnichenko, I. V.; Anslyn, E. V. Practical applications of supramolecular chemistry. *Chem. Soc. Rev.* **2017**, 46, 2385.

(16) Geng, W.-C.; Sessler, J. L.; Guo, D.-S. Supramolecular prodrugs based on host–guest interactions. *Chem. Soc. Rev.* **2020**, 49, 2303.

(17) Connors, K. A. The stability of cyclodextrin complexes in solution. *Chem. Rev.* **1997**, 97, 1325.

(18) Schneider, H.-J.; Hacket, F.; Rüdiger, V.; Ikeda, H. Nmr studies of cyclodextrins and cyclodextrin complexes. *Chem. Rev.* **1998**, 98, 1755.

(19) Inoue, Y. In *Annual reports on nmr spectroscopy*; Webb, G. A., Ed.; Academic Press: 1993; Vol. 27, p 59.

(20) Amado, A. M.; Ribeiro-Claro, P. J. A. Selection of substituted benzaldehyde conformers by the cyclodextrin inclusion process: A raman spectroscopic study. *J. Raman Spectrosc.* **2000**, 31, 971.

(21) Lamcharfi, E.; Kunesch, G.; Meyer, C.; Robert, B. Investigation of cyclodextrin inclusion compounds using ft-ir and raman spectroscopy. *Spectrochim. Acta, Part A* **1995**, 51, 1861.

(22) Perera, P.; Wyche, M.; Loethen, Y.; Ben-Amotz, D. Solute-induced perturbations of solvent-shell molecules observed using multivariate raman curve resolution. *J. Am. Chem. Soc.* **2008**, 130, 4576.

(23) Hu, M.-H. A.; Souza, L. E. S. d.; Lee, M.-R.; Ben-Amotz, D. Pressure and temperature-dependent gauche-trans isomerization of 1-bromopropane: Raman measurement and statistical thermodynamic analysis. *J. Chem. Phys.* **1999**, 110, 2498.

(24) Ben-Amotz, D. Hydration-shell vibrational spectroscopy. *J. Am. Chem. Soc.* **2019**, 141, 10569.

(25) Lawton, W. H.; Sylvestre, E. A. Self-modeling curve resolution. *Technometrics* **1971**, 13, 617.

(26) Davis, J. G.; Gierszal, K. P.; Wang, P.; Ben-Amotz, D. Water structural transformation at molecular hydrophobic interfaces. *Nature* **2012**, 491, 582.

(27) Wu, X.; Lu, W.; Streacker, L. M.; Ashbaugh, H. S.; Ben-Amotz, D. Temperature-dependent hydrophobic crossover length scale and water tetrahedral order. *J. Phys. Chem. Lett.* **2018**, 9, 1012.

(28) Yalkosky, S. H. H., Y.; Jain, P. *Handbook of aqueous solubility data*; Second Edition ed.; CRC Press: Boca Raton, FL.

(29) Frisch, M. J.; Trucks, G. W.; Schlegel, H. B.; Scuseria, G. E.; Robb, M. A.; Cheeseman, J. R.; Scalmani, G.; Barone, V.; Petersson, G. A., et al. *Gaussian 16*, Revision C.01; Gaussian, Inc.: Wallingford, CT, 2016

(30) Ogawa, Y.; Imazeki, S.; Yamaguchi, H.; Matsuura, H.; Harada, I.; Shimanouchi, T. Vibration spectra and rotational isomerism of chain molecules. Vii. 1-chloro-, 1-bromo-, and 1-iodopropanes, and 1-chloro-, 1-bromo-, and 1-iodobutanes. *Bull. Chem. Soc. Jpn.* **1978**, 51, 748.

(31) Durig, J. R.; Zhu, X.; Shen, S. Conformational and structural studies of 1-chloropropane and 1-bromopropane from temperature-dependant ft-ir spectra of rare gas solutions and ab initio calculations. *J. Mol. Struct.* **2001**, 570, 1.

(32) Marquez, C.; Nau, W. M. Polarizabilities inside molecular containers. *Angew. Chem., Int. Ed.* **2001**, 40, 4387.

(33) Yoshino, T.; Bernstein, H. J. Internal rotation: Ix. The infrared and raman spectra of liquid normal alkyl bromides. *Can. J. Chem.* **1957**, 35, 339.

(34) Katō, M.; Taniguchi, Y. Effect of pressure on conformational equilibria of liquid 1-chloropropane and 1-bromopropane. *J. Chem. Phys.* **1990**, 93, 4345.

(35) Kasezawa, K.; Kato, M. Effect of pressure on conformational equilibria of 1-chloropropane and 1-bromopropane in water and organic solvents: A raman spectroscopic study. *J. Phys. Chem. B* **2009**, 113, 8607.

(36) Groom, C. R.; Allen, F. H. The cambridge structural database in retrospect and prospect. *Angew. Chem. Int. Ed.* **2014**, 53, 662.

(37) Nicolis, I.; Villain, F.; Coleman, A. W.; Rango, C. d. X-ray crystallographic structure of the two-to-one α-cyclodextrin-acetone. 9h2o compound. *Supramol. Chem.* **1994**, 3, 251.

(38) Takashima, Y.; Sakamoto, K.; Oizumi, Y.; Yamaguchi, H.; Kamitori, S.; Harada, A. Complex formation of cyclodextrins with various thiophenes and their polymerization in water: Preparation of poly-pseudo-rotaxanes containing poly(thiophene)s. *J. Inclusion Phenom. Macrocyclic Chem.* **2006**, 56, 45.

(39) Choi, S.; Frank, W.; Ritter, H. Novel polymerization of diethyl fumarate and maleate in aqueous media via cyclodextrin-complexes. *React. Funct. Polym.* **2006**, 66, 149.

(40) Gu, Z. Y.; Guo, D. S.; Liu, Y. Guest releasing from solution to solid-state triggered by cyclomaltohexaose (alpha-cyclodextrin) aggregation. *Carbohydr. Res.* **2010**, 345, 2670.

(41) Sicard-Roselli, C.; Perly, B.; Le Bas, G. The respective benefits of x-ray crystallography and nmr for the structural determination of the inclusion complex between butyl-isothiocyanate and alpha-cyclodextrin. *J. Inclusion Phenom. Macrocyclic Chem.* **2001**, 39, 333.

(42) Noltemeyer, M.; Saenger, W. Topography of cyclodextrin inclusion complexes .12. Structural chemistry of linear alpha-cyclodextrin-polyiodide complexes - x-ray crystal-structures of (alpha-cyclodextrin)2.Lii3.I2.8h2o and (alpha-cyclodextrin)2.Cd0.5.I5.27h2o - models for the blue amylose-iodine complex. *J. Am. Chem. Soc.* **1980**, 102, 2710.

(43) Yoshiki, O.; Shuji, I.; Hiroko, Y.; Hiroatsu, M.; Issei, H.; Takehiko, S. Vibration spectra and rotational isomerism of chain molecules. Vii. 1-chloro-, 1-bromo-, and 1-iodopropanes, and 1-chloro-, 1-bromo-, and 1-iodobutanes. *Bull. Chem. Soc. Jpn.* **1978**, 51, 748.

(44) Anderson, M. W.; Taylor, J. A.; Walker, C. T. Energy difference of the trans–gauche c–br configurations in several 1-bromoalkanes. *J. Chem. Phys.* **1976**, 64, 2695.

(45) Tanabe, K.; Saëki, S. Vibrational frequencies, infrared absorption intensities and energy differences between rotational isomers of propyl halides. *J. Mol. Struct.* **1975**, 27, 79.

(46) Tanabe, K. Calculation of infrared band intensities and determination of energy differences of rotational isomers of 1,2-dichloro-, 1,2-dibromo- and 1-chloro-2-bromoethane. *Spectrochim. Acta, Part A* **1972**, 28, 407.

(47) Neugebauer, J.; Reiher, M.; Kind, C.; Hess, B. A., Quantum chemical calculation of vibrational spectra of large molecules—Raman and IR spectra for Buckminsterfullerene. *J. Comput. Chem.* **2002**, 23, 895.

(48) Yaws, C. L.; Satyro, M. A., Chapter 1 - Vapor Pressure – Organic Compounds. In *The Yaws Handbook of Vapor Pressure* Second Edition ed.

(49) Bruker (2018). Apex3, Saint, Bruker AXS Inc.: Madison (WI), USA.

(50) Krause, L.; Herbst-Irmer, R.; Sheldrick, G. M.; Stalke, D. Comparison of silver and molybdenum microfocus X-ray sources for single-crystal structure determination. *J. Appl. Cryst*. **2015**, 48, 3.

(51) a) SHELXTL suite of programs, Version 6.14, 2000-2003, Bruker Advanced X-ray Solutions, Bruker AXS Inc., Madison, Wisconsin: USA b) Sheldrick, G. M. A short history of SHELX. *Acta Crystallogr. A.* **2008**, 64, 112.

(52) Sheldrick GM. Crystal structure refinement with SHELXL. *Acta Crystallogr. C Struct. Chem.* **2015**, 71, 3.

(53) Hübschle, C. B.; Sheldrick, G. M.; Dittrich, B. ShelXle: a Qt graphical user interface for SHELXL. *J. Appl. Crystallogr.* **2011**, 44, 1281.

CHAPTER 4. SALTING OUT OF 1-HEXANOL, 2-HEXANOL, AND 1,2-HEXANEDIOL

4.1 Introduction

The influence of salts in the solubility of organic compounds in water is of great interest in different areas including atmospheric chemistry, organic process research and development, separation and extraction sciences, and biology.[1-6] In particular, the salting-out effect in water has been widely studied for solutes of different sizes and shapes, but the physical principles governing this phenomenon have yet to be established. The solubility of a compound in the presence of ions is dependent on its hydrophobic and hydrophilic segments as exemplified by experiments and simulations that have revealed specific interactions of ions with proteins.[7-11] Small molecules, including alkanes and alcohols, have also been previously investigated.[12-20] However, for small amphiphilic solutes, the effect of changing the position of a hydrophilic moiety or the addition of a second hydrophilic moiety, as well as the effect of self-aggregation have yet to be examined. Here, we do so by performing Raman multivariate curve resolution (Raman-MCR) spectroscopy to study the salting-out effect of 1-hexanol (1H), 2-hexanol (2H), and 1,2-hexanediol (12HD) in different aqueous ionic solutions. Our results indicate that changing the position of the hydrophilic group or the addition of a second hydrophilic group do not significantly alter the magnitude and trend of the salting-out effect of free amphiphilic species. Additionally, and more notably, we have experimentally quantified the salting out of 12HD micelles, and it appears be significantly smaller compared to that of free 12HD monomers, except for the systems on which HCl and HBr are present in the aqueous solvent. These results suggest that the alkali cations, excluding H^+, have a greater affinity to the 12HD micelle.

4.2 Methods

Preparation of Aqueous Solutions. Aqueous of 1H (1-hexanol, Sigma-Aldrich, 98%), 2H (2-hexanol, Acros Organics, 99%), 12HD (1,2-hexanediol, Sigma-Aldrich, 98%), KCl (potassium chloride, Sigma-Aldrich, 99%), NaCl (sodium chloride, Mallinckrodt Chemicals, 99%), LiCl (lithium chloride, Mallinckrodt Chemicals, 99%), HCl (hydrochloric acid,

Sigma-Aldrich, ACS 37%), and HBr (hydrobromic acid, Sigma-Aldrich, ACS 48%) were prepared with ultrapure filtered water (Milli Q UF Plus, Millipore, 18.2 MΩ cm).

Saturated solutions of 1H and 2H were prepared by layering the corresponding alcohol on top of the aqueous solvents. These samples were placed on an orbital shaker for a period of 72 hours to allow both alcohols to saturate the aqueous phase to their solubility limits. The solubilities of 1H and 2H are ~0.07 mol L^{-1} and 0.13 mol L^{-1}, respectively.[21]

For the preparation of 12HD two-phase systems, a 1-octanol (Sigma-Aldrich, 99%) layer was added on top of each 12HD aqueous solution. The volume of 1-octanol added corresponds to the volume of the aqueous solution. A layer of 1-octanol was also added on top of the aqueous solvents such that all of them included this component. All of the two-phase systems were placed on an orbital shaker for 72 hours to ensure equilibration.

Raman-MCR Spectroscopy. Raman spectra were obtained at 20°C using an Ar-ion 514.5 nm laser with ∼20 mW of power at the sample and 5 min integration time, as previously described.[18,22] The self-modeling curve resolution (SMCR) algorithm was used on pairs of solvent and solution spectra to obtain Raman-MCR solute-correlated (SC) spectra.[23-26] In these spectral decompositions, the solvent spectrum was constrained to either being pure water or that of the corresponding salt solution. For the SMCR analysis of 12HD two-phase systems, the aqueous solvents included 1-octanol dissolved to its solubility limit.

4.3 Results and Discussion

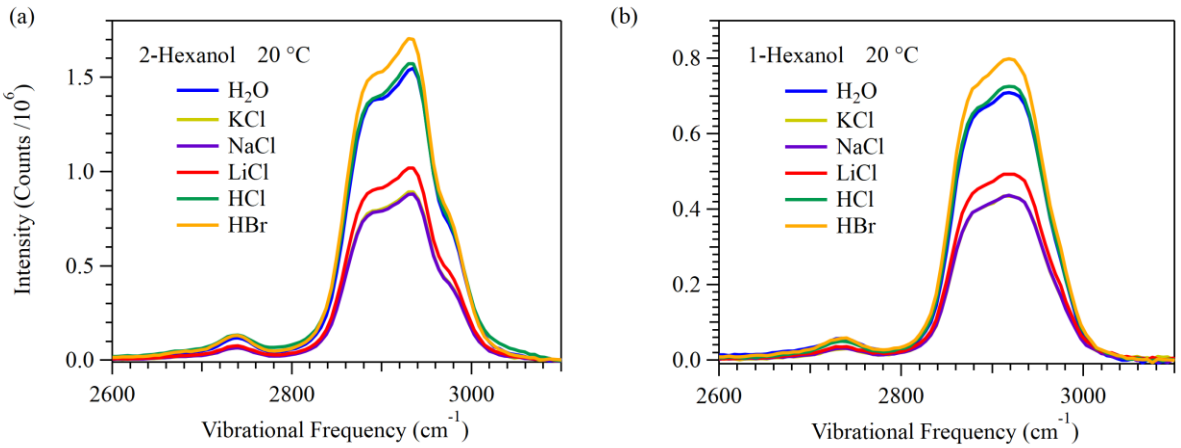

Figure 4-1. SC spectra of 2H (a) and 1H (b) dissolved in different aqueous solvents. The concentration of the salts and acids in the aqueous ionic solvents was 1 mol L^{-1}.

Figures 4-1 (a) and (b) show the effect of ions on the solubilities of both 2H and 1H. Specifically, they show how the areas of the C–H vibrational bands change when the cation size changes. Notice that for the alkali-cation series, when Cl^- is the counter ion, the C–H bands that decrease in intensity relative to that of pure water, correspond to the systems where K^+, Na^+, and Li^+ are the cations. The C–H band area decrease is the highest for the systems where the cation in the aqueous phase is either Na^+ or K^+ since they have identical C–H bands areas within the errors of the measurements. For the systems where Li^+ is the cation in the aqueous phase, the C–H band area decreases as well, but at a smaller magnitude. In contrast, when the cation is H^+, the C–H band area increases slightly compared to that of pure water, but within experimental error it is suggested that they are about the same. The effect of changing the counterion in the acid aqueous solutions was also tested. When the acid is HBr in the aqueous phase, the C–H peak area has a significant increment relative to that of pure water.

The C–H band areas in Figures 4-1 (a) and 4-1 (b) are proportional to the amount of free 2H and 1H that is dissolved in the aqueous phase assuming that the C–H Raman cross section of these molecules remains about the same under these different environments. By using the known concentration of 1H and 2H in water and the corresponding area under the curve, as a single point calibration, the solubilities in the aqueous ionic solvents were calculated and are listed in Table 4-1.

Table 4-1. Solubilities of 1H and 2H in different aqueous solvents. The concentration of salts and acids in the aqueous phase was 1 mol L^{-1}.

Aqueous Solvent	[2H] (mol L^{-1})	[1H] (mol L^{-1})
H_2O	0.126	0.065
KCl	0.072	0.040
NaCl	0.071	0.040
LiCl	0.083	0.046
HCl	0.133	0.066
HBr	0.138	0.073

For 2H and 1H the salting out coefficient, so-called Setschenow (or Setchenov) coefficient, (K) can be readily obtained from Equation 4-1, where c^{w}_{solute} and c^{is}_{solute} correspond to the concentration of the solute in pure water and the aqueous ionic solutions, respectively, and c^{is}_{salt} is the concentration of the corresponding salt or acid in the aqueous ionic solution.

$$K = \frac{RT \ln\left(\frac{c^{w}_{solute}}{c^{is}_{solute}}\right)}{c^{is}_{salt}} \quad (4\text{-}1)$$

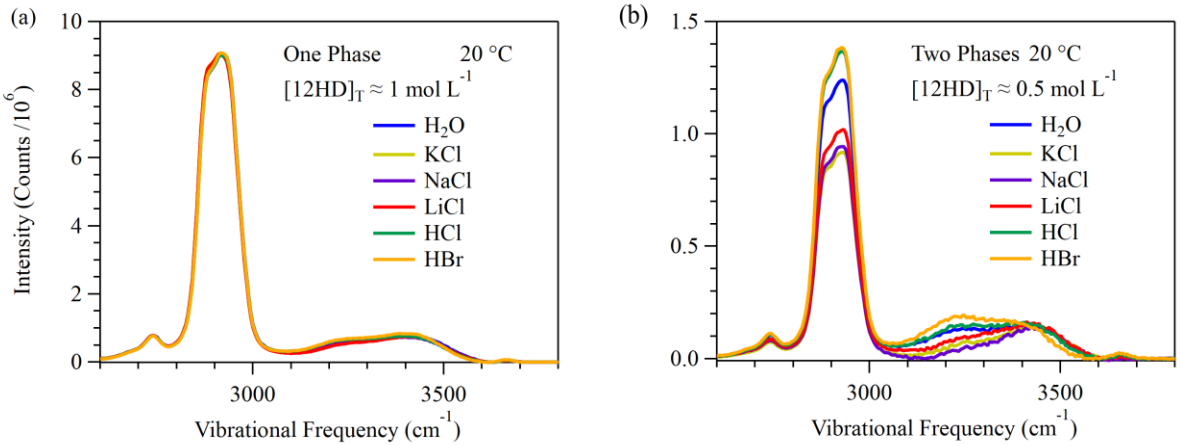

Figure 4-2. 12HD SC spectra obtained in single aqueous phases (a) and equilibrated aqueous octanol two phase (b) systems, all obtained starting with a 1 mol L^{-1} 12HD solutions. The concentration of the salts and acids in the aqueous phase was 1 mol L^{-1}.

Figures 4-2 (a) and (b) depict the SC spectra of 1 mol L^{-1} 12HD solutions without and with the addition of a 1-octanol layer on top. The change of the C–H band areas between (a) and (b) is

due to the partitioning of 12HD into the 1-octanol-rich phase after equilibration. The blue SC spectrum in Figure 4-2 (b) corresponds to the system where the aqueous layer is pure water. This spectrum cannot be used as reference in the K analysis since the associated two-phase system was the only one which formed a third phase between the aqueous and oil phases. Nevertheless, to overcome this difficulty, it is assumed that the green SC spectrum in Figure 4-2 (b), which is the spectrum of the system where 1mol L^{-1} HCl is the aqueous ionic solvent, can be used as the reference SC spectrum since the results in Figure 4-1 show that the SC spectra in both pure water and HCl are about the same. The yellow, purple, and red spectra in Figure 4-2 (b) result from salting out of 12HD and is more substantial in KCl and NaCl aqueous solutions. The SC spectrum shown in orange corresponds to the system on which HBr is present in the aqueous phase, and its presence does not to change the partitioning of free 12HD molecules.

For miscible solutes like 12HD, the solubility method described previously cannot be used for the determination of K. Instead, a partitioning strategy is carried out. The ratio of solute concentrations in pure water (c^{w}_{solute}) and 1-octanol phase (c^{o}_{solute}), also known as the water-octanol partitioning coefficient (P^{wo}_{solute}), can be obtained using Equation 4-2.

$$P^{wo}_{solute} = \frac{c^{w}_{solute}}{c^{o}_{solute}} \tag{4-2}$$

If c^{o}_{solute} is 1 mol L^{-1}, then $c^{w}_{solute} = P^{wo}_{solute}$ in mol L^{-1} units. Furthermore, when the solvent is an aqueous ionic solution, $c^{is}_{solute} = P^{iso}_{solute}$ in mol L^{-1} units if the concentration of the solute in the associated 1-octanol phase is 1 mol L^{-1}. By substituting these expressions into Equation 4-1, we obtain Equation 4-3 which allows the calculation of K from partitioning coefficients.

$$K = \frac{RT \ln\left(\frac{P^{wo}_{solute}}{P^{iso}_{solute}}\right)}{c^{is}_{salt}} \tag{4-3}$$

The C–H band areas in Figure 4-2 (b) are proportional to c^{w}_{solute} and c^{is}_{solute} of the different aqueous ionic solvents in the two-phase systems. Using the areas under the curves in Figure 4-2 (a), which correspond to a total concentration of 1 mol L^{-1}, c^{w}_{solute} and c^{is}_{solute} can be calculated. After

estimating the volumes in the two phases, followed by the analysis of the transfer of moles using the law of conservation of mass, the number of moles of the solute in the 1-octanol phase was determined. Once the concentrations in both phases are known the partitioning coefficients P^{wo}_{solute} and P^{iso}_{solute} can be calculated. The values of P^{iso}_{solute} are tabulated in Table 4-2 according to the nature of the aqueous ionic solvent. The P^{wo}_{solute} value determined this way is 0.182 and it can not be used for the determination of K due to the third phase that was formed in between the two phases. To overcome this issue, it was assumed that P^{wo}_{solute}= 0.198, which is P^{iso}_{solute} of the two-phase system on which HCl is in the aqueous ionic phase. This assumption is suggested after noticing that the solubilities of 1H and 2H are about the same in water and in 1 mol L^{-1} HCl.

Table 4-2. 12HD partitioning coefficients in different aqueous ionic solvents. The concentration of salts and acids in the aqueous phase was 1 mol L^{-1}.

Aqueous Phase	P^{iso}_{solute}
KCl	0.127
NaCl	0.132
LiCl	0.144
HCl	0.198
HBr	0.202

The Setschenow coefficient of aggregated 12HD species (K_n) can be determined by calculating ΔK from the measured influence of ions on the critical aggregate concentration according to Equation 4-4, where $\Delta cac_{solute} = cac^{is}_{solute} - cac^{w}_{solute}$.[18]

$$\Delta K = K_n - K = RT\left(\frac{\Delta cac_{solute}}{cac^{is}_{solute}\, c^{is}_{salt}}\right) \quad (4\text{-}4)$$

In the above expression, cac^{is}_{solute} and cac^{w}_{solute} are the critical aggregate concentrations of the solute in the presence and absence of ions in the aqueous solution. The cac^{w}_{solute} and cac^{is}_{solute} values for 12HD were obtained from a previous investigation and ongoing experiments our group is carrying out.[19] cac^{w}_{solute} is 0.7 mol L^{-1} while the cac^{is}_{solute} values are 0.45, 0.44, 0.49 mol L^{-1} for 1 mol L^{-1} KCl, NaCl, and LiCl aqueous solutions, respectively. For 2 mol L^{-1} NaCl, LiCl, HCl, and HBr aqueous solutions, cac^{is}_{solute} are 0.33, 0.41, 0.63, and 0.66 mol L^{-1}, respectively.

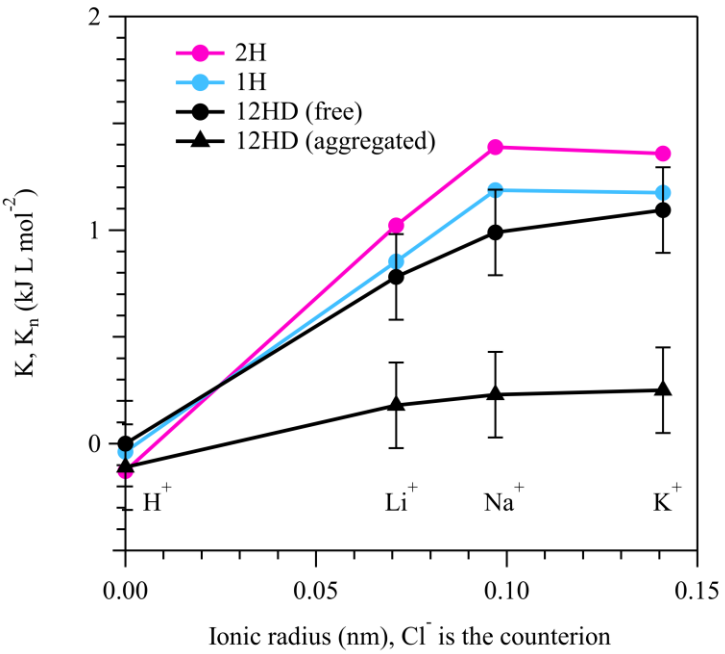

Figure 4-3. Salting out coefficients of 2H, 1H, 12HD (free), and 12HD (aggregated).

Figure 4-3 shows the dependence of K on the cation size for aqueous ionic systems where the counterion is Cl^-. Notice that for all the solutes studied the values of K are about the same when the cations are Na^+ and K^+ within the errors associated with experiments. Specifically, for 2H, K is ~1.4 kJ L mol^{-2}, while for 1H, K is ~1.2 kJ L mol^{-2}, and for free 12HD it has a value of ~1.0 ± 0.2 kJ L mol^{-2}. From these measurements, it is suggested that the salting out effect for all these solutes has a maximum when the cation is either Na^+ or K^+. For the case of Li^+, the values of K are ~1.0, 0.9, and 0.8 ± 0.2 kJ L mol^{-2} for 2H, 1H and free 12HD, respectively. When H^+ is the cation, the K coefficients are negative in the case of 2H and 1H. By using Equation 4-4, K_n values, which correspond to the salting out effect of aggregated 12HD, were determined and are ~0.3 ± 0.2, 0.2 ± 0.2, 0.2 ± 0.2, -0.1 ± 0.2, and -0.1 ± 0.2 kJ L mol^{-2} for KCl, NaCl, LiCl, HCl, and HBr, respectively. These results are also shown in Figure 4-3 and compared with K.

4.4 Conclusions

Raman-MCR spectroscopy was utilized to determine the influence of alkali-cations in the salting out effect of 1H, 2H, free 12HD, and aggregated 12HD. The effect of changing the position of the hydrophilic group or the addition of a second hydrophilic group do not significantly modify

the magnitude and trend of the salting-out effect of the free amphiphilic species investigated. It is generally observed that the salting-out effect goes through a maximum at Na^+. However, for all the solutes studied, the maximum occurs at both Na^+ and K^+. These results could be specific to these molecules which have approximately the same size and shape. Furthermore, we have experimentally quantified the salting out of 12HD micelles, which happens to be significantly smaller when compared to that of free 12HD monomers, except for the systems on which HCl and HBr are present in the aqueous solvent.

4.5 References

(1) Tompsett, G. A.; Boock, J. T.; DiSpirito, C.; Stolz, E.; Knutson, D. R.; Rivard, A. G.; Overdevest, M. R.; Conlon, C. N.; Prather, K. L. J.; Thompson, J. R.; Timko, M. T., Extraction Rate and Energy Efficiency of Supercritical Carbon Dioxide Recovery of Higher Alcohols from Dilute Aqueous Solution. *Energy Technol*. **2018**, 6, 683.

(2) Hyde, A. M.; Zultanski, S. L.; Waldman, J. H.; Zhong, Y.-L.; Shevlin, M.; Peng, F., General Principles and Strategies for Salting-Out Informed by the Hofmeister Series. *Org. Process Res. Dev*. **2017**, 21, 1355.

(3) Baldwin, R. L., How Hofmeister ion interactions affect protein stability. *Biophys. J.* **1996**, 71, 2056.

(4) Sargent, R.; Rieman, W., Salting-out Chromatography. I. Alcohols. *J. Phys. Chem*. **1957**, 61, 354.

(5) Dooley, K. M.; Cain, A. W.; Carl Knopf, F., Supercritical fluid extraction of acetic acid, alcohols and other amphiphiles from acid-water mixtures. *J. Supercrit. Fluids* **1997**, 11, 81.

(6) Marcolli, C.; Krieger, U. K., Phase Changes during Hygroscopic Cycles of Mixed Organic/Inorganic Model Systems of Tropospheric Aerosols. *J. Phys. Chem. A* **2006**, 110, 1881.

(7) Zhang, Y.; Cremer, P. S., Interactions between macromolecules and ions: the Hofmeister series. *Curr. Opin. Chem. Biol.* **2006**, 10, 658.

(8) Shimizu, S.; McLaren, W. M.; Matubayasi, N., The Hofmeister series and protein-salt interactions. *J. Chem. Phys.* **2006**, 124, 234905.

(9) Pegram, L. M.; Record, M. T., Thermodynamic Origin of Hofmeister Ion Effects. *J. Phys. Chem. B* **2008**, 112, 9428.

(10) Lo Nostro, P.; Ninham, B. W., Hofmeister Phenomena: An Update on Ion Specificity in Biology. *Chem. Rev.* **2012**, 112, 2286.

(11) Okur, H. I.; Hladílková, J.; Rembert, K. B.; Cho, Y.; Heyda, J.; Dzubiella, J.; Cremer, P. S.; Jungwirth, P., Beyond the Hofmeister Series: Ion-Specific Effects on Proteins and Their Biological Functions. *J. Phys. Chem. B* **2017**, 121, 1997.

(12) Katsuto, H.; Okamoto, R.; Sumi, T.; Koga, K., Ion Size Dependences of the Salting-Out Effect: Reversed Order of Sodium and Lithium Ions. *J. Phys. Chem. B* **2021**, 125, 6296.

(13) Long, F. A.; McDevit, W. F., Activity Coefficients of Nonelectrolyte Solutes in Aqueous Salt Solutions. *Chem. Rev.* **1952**, 51, 119.

(14) Weisenberger, S.; Schumpe, A., Estimation of gas solubilities in salt solutions at temperatures from 273 K to 363 K. *AIChE J.* **1996**, 42, 298.

(15) Clever, H. L., Setchenov salt-effect parameter. *J. Chem. Eng. Data* **1983**, 28, 340.

(16) Graziano, G., On the Salting Out of Benzene by Alkali Chlorides. *J. Chem. Eng. Data* **2009**, 54, 464.

(17) Ganguly, P.; Hajari, T.; van der Vegt, N. F. A., Molecular Simulation Study on Hofmeister Cations and the Aqueous Solubility of Benzene. *J. Phys. Chem. B* **2014**, 118, 5331.

(18) Mendes de Oliveira, D.; Ben-Amotz, D., Spectroscopically Quantifying the Influence of Salts on Nonionic Surfactant Chemical Potentials and Micelle Formation. *J. Phys. Chem. Lett.* **2021**, 12, 355.

(19) Francisco, O. A.; Glor, H. M.; Khajehpour, M., Salt Effects on Hydrophobic Solvation: Is the Observed Salt Specificity the Result of Excluded Volume Effects or Water Mediated Ion Hydrophobe Association? *Chemphyschem* **2020**, 21, 484.

(20) Desnoyers, J. E.; Billon, M.; Léger, S.; Perron, G.; Morel, J.-P., Salting out of alcohols by alkali halides at the freezing temperature. *J. Solution Chem.* **1976**, 5, 681.

(21) Stephenson, R.; Stuart, J.; Tabak, M., Mutual solubility of water and aliphatic alcohols. *J. Chem. Eng. Data* **1984**, 29, 287.

(22) Davis, J. G.; Gierszal, K. P.; Wang, P.; Ben-Amotz, D., Water structural transformation at molecular hydrophobic interfaces. *Nature* **2012**, 491, 582.

(23) Perera, P.; Wyche, M.; Loethen, Y.; Ben-Amotz, D., Solute-Induced Perturbations of Solvent-Shell Molecules Observed Using Multivariate Raman Curve Resolution. *J. Am. Chem. Soc.* **2008**, 130, 4576.

(24) Ben-Amotz, D., Hydration-Shell Vibrational Spectroscopy. *J. Am. Chem. Soc.* **2019**, 141, 10569.

(25) Lawton, W. H.; Sylvestre, E. A., Self Modeling Curve Resolution. *Technometrics* **1971**, 13, 617.

(26) Ben-Amotz, D.; Mendes de Oliveira, D., Surfactant aggregate size distributions above and below the critical micelle concentration. *J. Chem. Phys.* **2021**, 155, 224902.

VITA

Andres S. Urbina was born in 1992 in Quito, Ecuador. He graduated from the International Baccalaureate (IB) Programme and Unidad Educativa Municipal Sebastián de Benalcázar in 2010. During the IB programme period, his passion for chemistry and physics emerged. He attended Universidad San Francisco de Quito and graduated *Cum Laude* with a B.Sc. in Chemistry. Andres joined Purdue University in 2017 and earned his Ph.D. in Chemistry.

LIST OF PUBLICATIONS

(1) Bredt, A. J.; Kim, Y.; Mendes de Oliveira, D.; **Urbina, A. S.**; Slipchenko L. V.; Ben-Amotz D., Expulsion of Hydroxide Ions from Methyl Hydration Shells. *J. Phys. Chem. B* **2022**, 126, 869.

(2) Bredt, A. J.; Mendes de Oliveira, D.; **Urbina, A. S.**; Slipchenko L. V.; Ben-Amotz D., Hydration and Seamless Integration of Hydrogen Peroxide in Water. *J. Phys. Chem. B* **2021**, 125, 6986.

(3) **Urbina, A. S.**; Boulos, V. M.; Mendes de Oliveira, D.; Zeller, M.; Ben-Amotz D., Binding Induced Unfolding of 1-Bromopropane in α-Cyclodextrin. *J. Phys. Chem. B* **2020**, 124, 11015.

(4) Morawietz, T.; **Urbina, A. S.**; Wise, P. K.; Wu, X.; Lu, W.; Ben-Amotz, D.; Markland, T. E., Hiding in the Crowd: Spectral Signatures of Overcoordinated Hydrogen-Bond Environments. *J. Phys. Chem. Lett.* **2019**, 10, 6067.

(5) Jimenez-Uzcategui, G. V., Rommel L.; **Urbina, A. S.**; Egas, David A.; Garcia, Carolina; Cotin, Javier; Sevilla, Christian, Lead and cadmium levels in Galapagos penguin *Spheniscus mendiculus*, flightless cormorant *Phalacrocorax harrisi*, and waved albatross *Phoebastria irrorata*. *Mar. Ornithol*. **2017**, 45, 159.

(6) **Urbina, A. S.**; Zambrano, C. H.; Torres, F. J.; Rincon, L., Insights on the aromaticity of imidazolylidene carbenes by means of DFT calculations. *Comput. Theor. Chem.* **2016**, 1094, 108.

(7) **Urbina, A. S.**; Torres, F. J.; Rincon, L., The electron localization as the information content of the conditional pair density. *J. Chem. Phys.* **2016**, 144, 244104.

(8) Posligua, V.; **Urbina, A. S.**; Rincon, L.; Soetens, J. C.; Mendez, M. A.; Zambrano, C. H.; Torres, F. J., Theoretical evaluation of metal-functionalized *rccc*-R-pyrogallol[4]arenes as media for molecular hydrogen storage. *Comput. Theor. Chem.* **2015**, 1073, 75.

(9) Rodriguez, C. G.; **Urbina, A. S.**; Torres, F. J.; Cazar, D.; Ludeña, E. V., Non-Born-Oppenheimer nuclear and electronic densities for a three-particle Hooke-Coulomb model. *Comput. Theor. Chem.* **2013**, 1018, 26.

(10) **Urbina, A. S.**; Saltos, A. A.; Torres, F. J., Estudio computacional B3LYP de la interacción del hidrógeno molecular con *rccc*-R-Pyg[4]arenos [R = metil, fluor] funcionalizados con Li^+. *Avances en Ciencias e Ingenierías* **2011**, 3.